

Modeling a disease-correlated tubulin mutation in budding yeast reveals insight into MAP-mediated dynein function

E. Denarier^{a,†}, K. H. Ecklund^{b,†}, G. Berthier^a, A. Favier^a, E. T. O'Toole^c, S. Gory-Fauré^a, L. De Macedo^a, C. Delphin^a, A. Andrieux^a, S. M. Markus^{b,†,*}, and C. Boscheron^{a,†,*}

^aUniversité Grenoble Alpes, Commissariat à l'énergie atomique et aux énergies alternatives, Centre national de la recherche scientifique, Grenoble institut des neurosciences, Institut de biologie structurale, Institut national de la santé et de la recherche médicale, Institut de recherche interdisciplinaire de Grenoble, F-38000 Grenoble, France;

^bDepartment of Biochemistry and Molecular Biology, Colorado State University, Fort Collins, CO 80523; ^cDepartment of Molecular, Cellular, and Developmental Biology, University of Colorado, Boulder, Boulder, CO 80302

ABSTRACT Mutations in the genes that encode α - and β -tubulin underlie many neurological diseases, most notably malformations in cortical development. In addition to revealing the molecular basis for disease etiology, studying such mutations can provide insight into microtubule function and the role of the large family of microtubule effectors. In this study, we use budding yeast to model one such mutation—Gly436Arg in α -tubulin, which is causative of malformations in cortical development—in order to understand how it impacts microtubule function in a simple eukaryotic system. Using a combination of *in vitro* and *in vivo* methodologies, including live cell imaging and electron tomography, we find that the mutant tubulin is incorporated into microtubules, causes a shift in α -tubulin isotype usage, and dramatically enhances dynein activity, which leads to spindle-positioning defects. We find that the basis for the latter phenotype is an impaired interaction between She1—a dynein inhibitor—and the mutant microtubules. In addition to revealing the natural balance of α -tubulin isotype utilization in cells, our results provide evidence of an impaired interaction between microtubules and a dynein regulator as a consequence of a tubulin mutation and sheds light on a mechanism that may be causative of neurodevelopmental diseases.

Monitoring Editor

Thomas Surrey
Centre for Genomic Regulation

Received: May 12, 2021

Revised: Aug 3, 2021

Accepted: Aug 5, 2021

This article was published online ahead of print in MBoC in Press (<http://www.molbiolcell.org/cgi/doi/10.1091/mbc.E21-05-0237>).

[†]These authors contributed equally to this work.

*Address correspondence to: Cécile Boscheron (cecile.boscheron@ibs.fr); Steven Markus (steven.markus@colostate.edu).

Abbreviations used: AD, activation domain; CV, column volumes; DBD, DNA binding domain; DTT, dithiothreitol; EGTA, ethylene glycol-bis(2-aminoethyl)ether-*N,N,N',N'*-tetraacetic acid; EM, electronic microscopy; EM-CCD, electron multiplying charge coupled device; 5-FOA, 5-fluoroorotic acid; GFP, green fluorescent protein; HU, hydroxyurea; IPTG, isopropyl β -D-1-thiogalactopyranoside; IRM, Interference reflection microscopy; LC/MS, liquid chromatography/ mass spectrometry; MAP, microtubule-associated protein; MCD, malformations of cortical development; NA, numerical aperture; P-A, pre-anaphase; PIPES, piperazine-*N,N'*-bis(2-ethanesulfonic acid); PM buffer, PIPES MgCl₂ buffer; PVDF, polyvinylidene fluoride; RFP, red fluorescent protein; SD, synthetic defined media; SDS-PAGE, sodium dodecyl sulfate-polyacrylamide gel electrophoresis; SPB, spindle pole body; TFA, tri fluoro acetic acid; TIRF, total internal reflection fluorescence microscopy; YFP, yellow fluorescent protein; YPAD, yeast extract peptone adenine dextrose.

© 2021 Denarier et al. This article is distributed by The American Society for Cell Biology under license from the author(s). Two months after publication it is available to the public under an Attribution–Noncommercial–Share Alike 3.0 Unported Creative Commons License (<http://creativecommons.org/licenses/by-nc-sa/3.0>). "ASCB®," "The American Society for Cell Biology®," and "Molecular Biology of the Cell®" are registered trademarks of The American Society for Cell Biology.

INTRODUCTION

Microtubules and their effectors play numerous critical roles during the life of a cell. For example, in addition to providing tracks for polarized motor-mediated vesicular transport, they comprise the mitotic spindle and are key effectors of nuclear and neuronal migration during early brain development. As a consequence of their myriad cellular roles, it is unsurprising that mutations in the genes that encode α - and β -tubulin and many microtubule-associated proteins (MAPs) are causative of human diseases, with those correlating with tubulin mutations known as tubulinopathies. Most prominent among them are neurological diseases, such as the malformations of cortical development (MCD) family of developmental brain disorders (Bahi-Buisson and Cavallin, 1993; Jaglin et al., 2009; Poirier et al., 2010, 2013; Breuss et al., 2012; Cushion et al., 2014; Di Donato et al., 2018; Fourel and Boscheron, 2020). MCD diseases (e.g., lissencephaly, pachygyria, and polymicrogyria), which are characterized by severe brain malformations, are largely a consequence of defective neuronal migration in the developing brain.

Mutations in TUBA1A (tubulin α -subunit 1A isoform), which encodes a common α -tubulin isoform expressed in mammalian cells, account for most tubulinopathies and for 4–5% of all lissencephaly cases (Morris-Rosendahl *et al.*, 2008; Di Donato *et al.*, 2018). A total of 121 unique heterozygous diseasecausing mutations have been identified in TUBA1A, of which only 15 were found in more than one patient, with the remaining 106 identified only in individuals (Hebebrand *et al.*, 2019). Although the molecular basis for disease etiology in most patients remains unknown, a recent study predicted that the majority of mutations compromise protein folding and interaction with effectors (Hebebrand *et al.*, 2019). In addition to providing insight into disease pathology, studying such mutations can reveal molecular insight into the cellular role of microtubules and their effectors (Fourel and Boscheron, 2020).

One residue that is mutated in at least two patients (both of whom are heterozygous for the mutation) is glycine 436 (to an arginine or aspartate), which maps to a region that is directly adjacent to the unstructured C-terminal domain of α -tubulin, a region that is important for interactions with a wide range of MAPs that are critical for various microtubule processes (Bahi-Buisson *et al.*, 2008; Hebebrand *et al.*, 2019; Fourel and Boscheron, 2020). The unstructured C-termini of α - and β -tubulin are enriched in negatively charged amino acids, most commonly glutamate (see Figure 1B). These acidic tubulin “tails” (also known as “E-hooks” for their enrichment in glutamates) are required for the normal binding and function of numerous MAPs, including kinetochore-associated factors (e.g., Ndc80, Dam1) (Westermann *et al.*, 2005; Ciferri *et al.*, 2008), microtubule effectors (e.g., spastin, XMAP215) (Brouhard *et al.*, 2008; Eckert *et al.*, 2012), end-binding proteins (e.g., Bik1/CLIP-170) (Bieling *et al.*, 2008; Caudron *et al.*, 2008), and molecular motors (e.g., kinesin, dynein) (Sirajuddin *et al.*, 2014). Given the proximity of G436R to the α -tubulin E-hook, we reasoned that this mutation might disrupt microtubule function in part by perturbing this region. Thus, we chose to employ a simple model system to assess the consequences of this mutation on microtubule function.

Studying tubulin mutations in mammalian cells is complicated by the fact that numerous isoforms of α - and β -tubulin are present in the human genome (nine α -tubulin, and ten β -tubulin isoforms) (Khodiyar *et al.*, 2007; Findeisen *et al.*, 2014). Each of these has a distinct expression pattern, and thus every cell’s tubulin content is a composite mixture of these many variants. In contrast to higher eukaryotes, things are much simpler in the budding yeast *Saccharomyces cerevisiae* in which ~70–90% of α -tubulin has been reported to be expressed from the essential *TUB1* gene, with the remaining ~10–30% arising from the *TUB3* gene (Schatz *et al.*, 1986b; Bode *et al.*, 2003; Gartz Hanson *et al.*, 2016). In addition to its simplicity, the mechanisms and effectors of spindle orientation (e.g., dynein, LIS1) and microtubule dynamics and function (e.g., tubulin, EB1, CLIP-170, ChTOG) are highly conserved between humans and budding yeast. In this organism, it is critical that the mitotic spindle is correctly oriented along the mother–bud axis and positioned in close proximity to the bud neck before mitotic exit; otherwise cell viability is compromised. The importance of these processes for cell viability permitted the use of genetic screens that revealed the presence of two distinct pathways that affect spindle orientation and position: namely, the Kar9/actomyosin and dynein pathways (Miller and Rose, 1998). The Kar9/actomyosin pathway relies on a microtubule guidance mechanism, whereby a microtubule plus end–associated myosin (Myo2) orients the mitotic spindle along the mother–bud axis (Lee *et al.*, 2000; Yin *et al.*, 2000; Hwang *et al.*, 2003). Myo2 is recruited to microtubule plus ends by the concerted effort of Kar9 (homologue of human adenomatous polyposis coli tumor suppressor;

APC) and the autonomous microtubule plus end–tracking protein, Bim1 (homologue of human EB1). Recently, we have modeled the disease-correlated TUBB2B F265L β -tubulin mutation in budding yeast and found that this mutation specifically compromises the Kar9/actomyosin pathway by disrupting the plus end localization of Bim1 (Denarier *et al.*, 2019).

Cytoplasmic dynein, on the other hand, functions from the cell cortex, from where Num1-anchored motors walk along microtubules emanating from spindle pole bodies (SPBs, the equivalent of centrosomes), which results in the positioning of the preanaphase spindle at the mother–bud neck (Li *et al.*, 1993; Carminati and Stearns, 1997; Heil-Chapdelaine *et al.*, 2000). Dynein is delivered to Num1 receptor sites at the bud cortex by a two-step “offloading” mechanism: 1) microtubule plus end–associated Bik1 (homologue of human CLIP170) recruits dynein-Pac1 (homologue of human Lis1) complexes to dynamic plus ends (Lee *et al.*, 2003; Sheeman *et al.*, 2003; Badin-Larcon *et al.*, 2004; Caudron *et al.*, 2008); 2) plus end–associated dynein, which appears to be inactive (Lammers and Markus, 2015), is delivered, or “offloaded,” to cortical Num1 receptor sites along with its effector complex, dynactin (Markus and Lee, 2011). Dynein activity is largely governed by its localization to these sites; however, at least one known MAP also regulates dynein activity in yeast: She1. The precise mechanism by which it does so in cells is currently unclear; however, *in vitro* studies show that She1 can reduce dynein velocity through simultaneous interactions with both microtubules and dynein (Ecklund *et al.*, 2017), whereas live cell studies have shown that She1 plays a role in polarizing dynein-mediated spindle movements toward the daughter cell (Markus *et al.*, 2012), perhaps in part by tuning dynactin recruitment to plus end–associated dynein (Woodruff *et al.*, 2009; Markus *et al.*, 2011). Of note, She1 binding to microtubules, and its effects on dynein motility, also requires the tubulin E-hooks (Markus *et al.*, 2012; Ecklund *et al.*, 2017).

To gain insight into the role and importance of α -tubulin G436 (hereafter referred to as G437, due to its position in yeast α -tubulin) and how it might affect the above processes, we produced *S. cerevisiae* yeast strains in which the native *TUB1* locus was replaced with the G437R mutant allele (*tub1*^{G437R}). Our results show that this mutation leads to alterations in tubulin isotype usage in cells, microtubule dynamics, and a spindle-positioning defect that is due to dysregulated dynein function. The dynein dysfunction phenotype is not a consequence of its mislocalization but is due to the reduced affinity of She1 for the mutant microtubules. Our data suggest that the presence of low copies of the mutant Tub1 α -tubulin protein in microtubules exerts allosteric, long-range effects on microtubule structure that lead to cooperative disruption of She1–microtubule binding yet protects cells against the severe morphological defects that arise in cells expressing only the compensatory Tub3 α -tubulin isotype. Although there is no clear She1 homologue in higher eukaryotes, we hypothesize that this mutation might interfere with dynein function in humans by disrupting the microtubule-binding behavior of a regulatory MAP, thus leading to neuronal physiological deficits and a consequent disruption of cerebral cortex development.

RESULTS

TUB1^{G437R} leads to an enhancement in microtubule dynamics during G2/M

Glycine 436 of TUBA1A (α -tubulin) is conserved among α -tubulins from numerous organisms, including budding yeast (*TUB1*; overall 74.1% identity between human TUBA1A and yeast Tub1). Glycine 436 (Figure 1A, red sphere) is one of three highly conserved small,

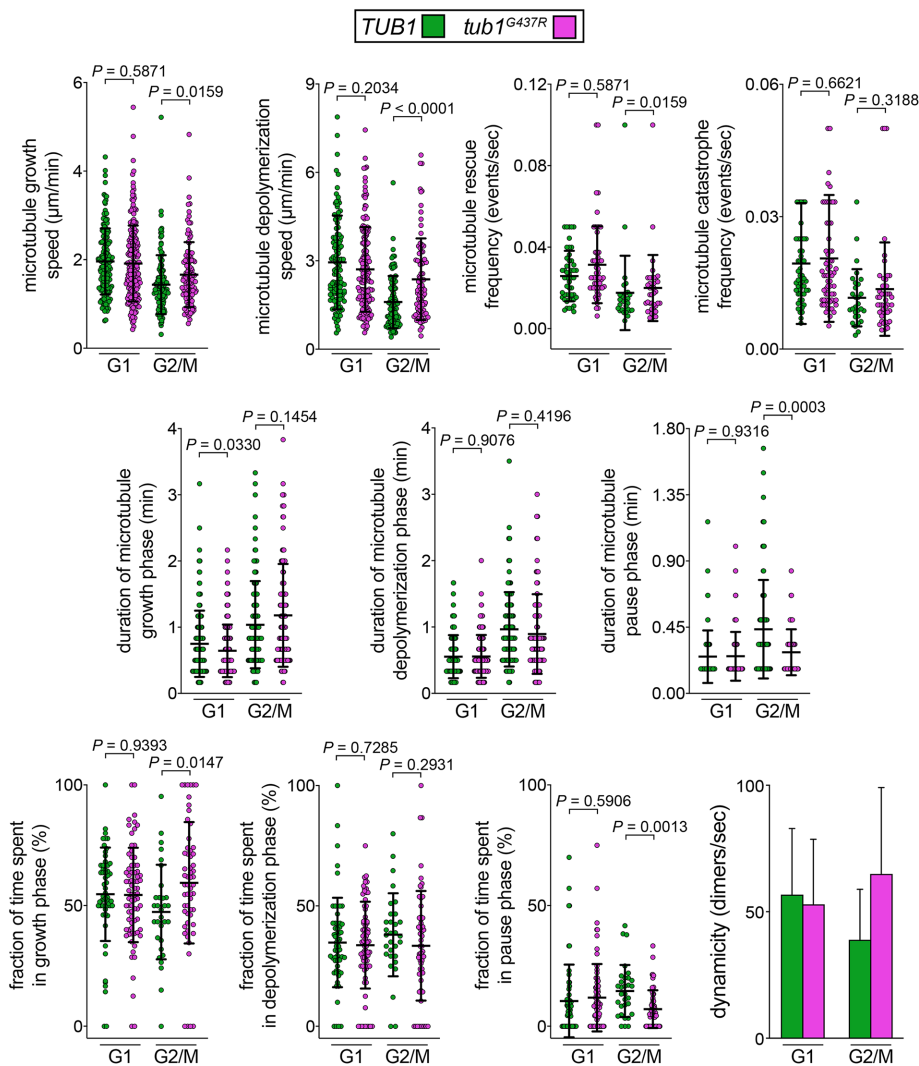


FIGURE 2. *tub1^{G437R}* cells exhibit altered microtubule dynamics during G2/M phase. Plots depicting the indicated microtubule dynamics parameters in the indicated phase of the cell cycle (as determined by cell and spindle morphology). Microtubule behavior was tracked over time using Bik1-GFP as a reporter (localizes prominently to the spindle, to various degrees along microtubules, and at microtubule plus ends). For each cell a single microtubule was used for dynamics measurements ($n = 41$ and 42 microtubules—from the same number of cells—from G1 *TUB1* and *tub1^{G437R}* cells, respectively, and $n = 31$ and 53 microtubules/cells from G2/M *TUB1* and *tub1^{G437R}*, respectively). With the exception of the dynamicity plot (showing mean values with SDs), all plots depict all data points (scatter plots) along with mean and SDs (bars). P values were calculated using an unpaired Welch's t test.

microtubules spent in their growth phase and a concomitant reduction in the relative fraction of time spent in pause in the mutant cells. This resulted in an overall increase in microtubule dynamicity (Toso *et al.*, 1993) (Figure 2), which may account for the enhanced sensitivity of the mutant cells to the depolymerizing agent, benomyl. Finally, although the mean microtubule length did not significantly differ between the two strains in G2/M (Supplemental Figure S3A), we noted that the mutant cells exhibited a larger fraction of long microtubules (38% of microtubules were $\geq 7 \mu\text{m}$ in *tub1^{G437R}* cells vs. 10% in wild-type cells; Supplemental Figure S3B), many of which extended from one cell compartment to the other (also see below). Taken together, these data suggest that the G437R mutation alters microtubule function in a manner suggestive of E-hook disruption.

chromosome segregation defects, reduced viability) that were not apparent by live cell imaging (see Figure 1C) or cell viability (see Figure 1D, "YPAD"), we focused on the latter possibility. To this end, we measured the fluorescence intensity of mRuby2-Tub1 (wild type or G437R) and mRuby2-Tub3 in both the mitotic spindle and individual astral microtubules in either wild-type or *tub1^{G437R}* cells. We used identical imaging conditions (e.g., laser power, camera exposure) to quantitatively compare the relative incorporation of mRuby2-Tub1 and mRuby2-Tub3 into these microtubule structures. Consistent with our immunoblotting data, this revealed that Tub1 and Tub3 comprise roughly equal proportions of microtubules in wild-type (*TUB1*) cells (Figure 3, C and D); however, these values differed significantly in *tub1^{G437R}* cells, in which Tub1^{G437R} incorporation into microtubules was reduced by 40 and 61% in astral and

Reduced Tub1^{G437R} expression levels are compensated by Tub3 isotype

We next wondered whether the G437R mutation leads to alterations in α -tubulin levels in cells. To this end, we measured relative protein content via immunoblot (using two different antibodies that recognize α -tubulin: 4A1 and YL1/2), which revealed a significant reduction in total α -tubulin in the mutant cells (30.6–42.7% reduction, determined with 4A1 and YL1/2, respectively; Figure 3, A and B).

In addition to *TUB1*, budding yeast possess a second α -tubulin gene encoded by *TUB3*. Whereas *TUB1* is reported to be the major α -tubulin isotype and is required for cell viability, cells tolerate deletion of *TUB3*, which possesses 91% identity and 95% similarity with *TUB1* (Schatz *et al.*, 1986a). Although previous studies estimated that Tub3 accounts for roughly ~10–30% of the cell's α -tubulin content (Bode *et al.*, 2003; Gartz-Hanson *et al.*, 2016), we sought to assess this with our yeast strains and immunoblotting techniques. To this end, we assessed α -tubulin levels in *tub3 Δ* mutants, in which all α -tubulin is encoded by *TUB1*. Interestingly, this revealed a 64.2% reduction in total α -tubulin content as a consequence of Tub3 deletion. We noted a similarly large reduction in total α -tubulin levels using the YL1/2 antibody (36.9%). This suggests that Tub3 comprises a larger proportion of tubulin in cells (~36–63%) than previously reported.

We reasoned that the reduction in α -tubulin levels as a result of the G437R mutation would lead to two possible situations in mutant cells: 1) a reduction in the length or number of cytoplasmic and spindle microtubules, or 2) an increase in the levels of Tub3 incorporation into microtubules to compensate for the Tub1 reduction. Because we noted no reduction in astral microtubule number or length (Supplemental Figure S3) and a reduced overall microtubule mass (scenario 1 above) would likely lead to severe physiological consequences (e.g.,

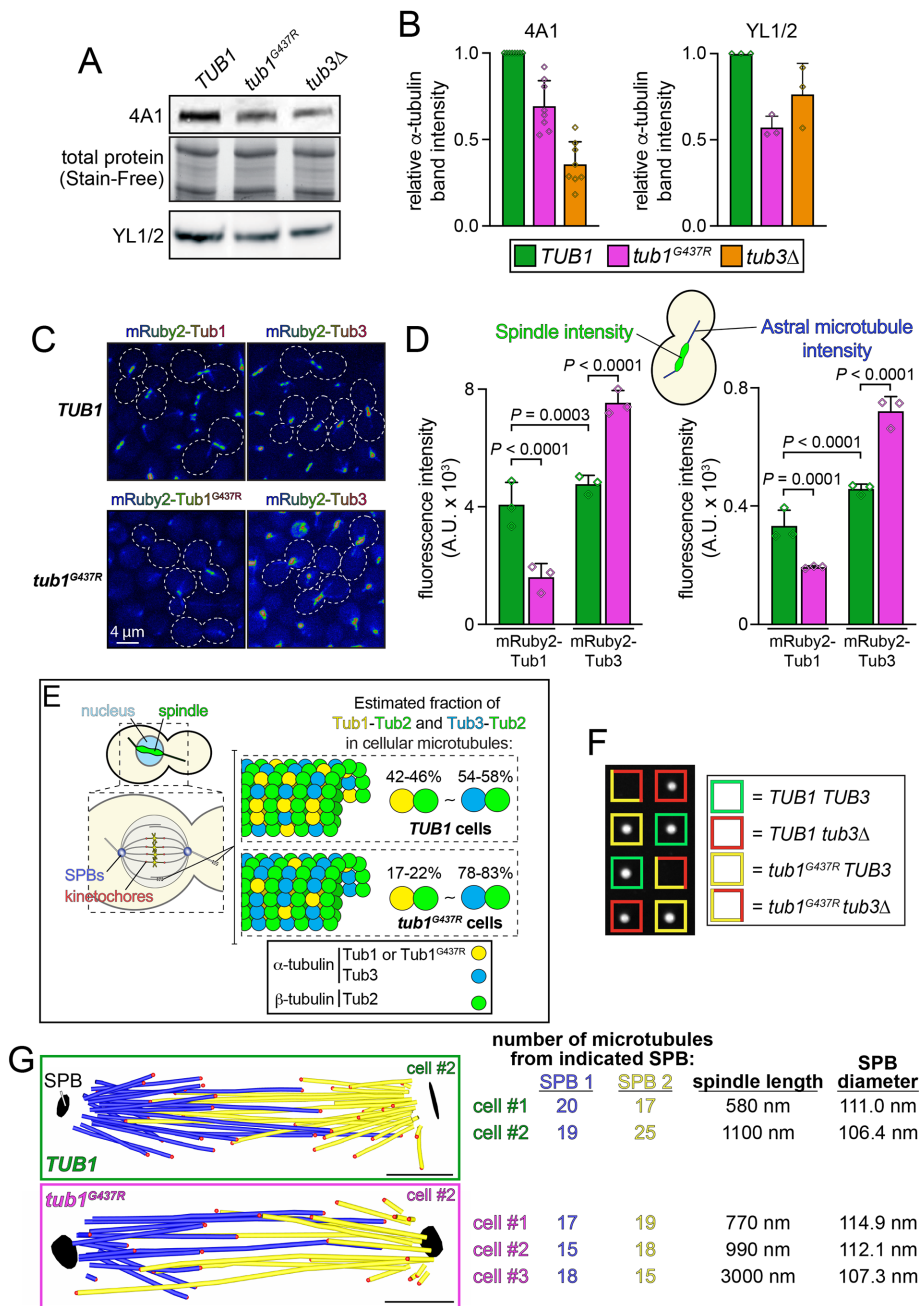


FIGURE 3: Tub1^{G437R} leads to changes in α-tubulin isotype usage in cells. (A) Representative immunoblots depicting relative α-tubulin expression in yeast strains with the indicated genotype. Lysates prepared from independent log phase cultures were separated by SDS-PAGE, transferred to PVDF, and then probed with either 4A1 or YL1/2 monoclonal antibodies, as indicated ($n = 8$ cell lysates prepared from independent cell cultures for 4A1 blot and $n = 3$ independent cell lysates for the YL1/2 blot). Before transfer, acrylamide gels were imaged for total protein (using Stain-Free technology; Bio-Rad) to normalize for potential differences in sample loading. (B) Plots depicting relative band intensities (mean \pm SD) of α-tubulin measured from immunoblots. Diamonds represent values obtained from each independent replicate experiment. Note that α-tubulin levels in *tub3Δ* cells varied across the three replicates (from 0.56 to 0.92) for immunoblots processed with the YL1/2 antibody (in contrast to those processed with 4A1). (C, D) Representative fluorescence images (C; shown as a heatmap) and quantitation (D) depicting the relative intensity of mRuby2-Tub1 (wild type or mutant) or mRuby2-Tub3 in either spindle (left) or astral microtubules (right) in wild-type or mutant cells. Before imaging, cells were arrested with 200 mM hydroxyurea (HU) for 2.5 h (to enrich for cells with mitotic spindles) and then mounted on agarose pads containing HU for fluorescence microscopy (for data sets from left to right, $n = 104, 106, 100,$ and 97 spindles and $n = 108, 62, 98,$ and 90 astral microtubules from three biological replicates each, respectively; P values were

spindle microtubules, respectively, and Tub3 levels were increased by 55 and 58% in astral and spindle microtubules, respectively. Thus, the reduction of Tub1^{G437R} incorporation into cellular microtubules is entirely offset by a compensatory incorporation of Tub3 (Figure 3E), leading to a situation in which the overall microtubule mass likely remains unchanged.

Given the apparent compensation of Tub3 for *tub1^{G437R}* in mutant cell microtubules, we wondered whether cells could tolerate expressing only Tub1^{G437R} in the absence of Tub3. To this end, we generated heterozygous *TUB1/tub1^{G437R} TUB3/tub3Δ* diploid cells, sporulated them, and assessed the viability of the recovered single- and double-mutant progeny. Although the single mutants exhibited normal colony morphology, none of the double mutants was viable (12 out of 12 expected double mutants from 24 tetrads were inviable), revealing that expression of only Tub1^{G437R} leads to cell death (Figure 3F). Although the reason for the inviability of the double mutants is unclear, it suggests that either microtubules cannot be assembled from only the mutant α-tubulin protein or microtubules assembled from only the mutant α-tubulin protein do not support proper cellular function.

To determine whether mitotic spindles assembled in *tub1^{G437R}* cells exhibit normal morphological characteristics (e.g., numbers and arrangements of microtubules), we compared the spindle organization between wild-type and mutant cells using electron tomography. Asynchronous cell cultures were collected and subjected to high-pressure freezing. Serial sections of cells with mitotic spindles were imaged by electron microscopy, and the microtubules were modeled from tomographic volumes, as

calculated using an unpaired Welch's t test). Diamonds represent values from independent biological replicates, and bars indicate mean \pm SD. (E) Cartoon depicting the relative balance of Tub1-Tub2:Tub3-Tub2 in wild-type and mutant microtubules. (F) Representative image of colonies (grown on YPAD) from a tetrad dissection depicting the synthetic lethal interaction between *tub1^{G437R}* and *tub3Δ*. Two representative tetrads are shown. (G) Models of spindle microtubules built from EM tomographic volumes from a pre anaphase wild type (*TUB1*) and mutant cell, along with parameters determined. Blue and yellow lines depict microtubules emanating from SPB1 and SPB2, respectively, red spheres depict microtubule plus ends, and black disks depict SPBs (scale bar, 200 nm).

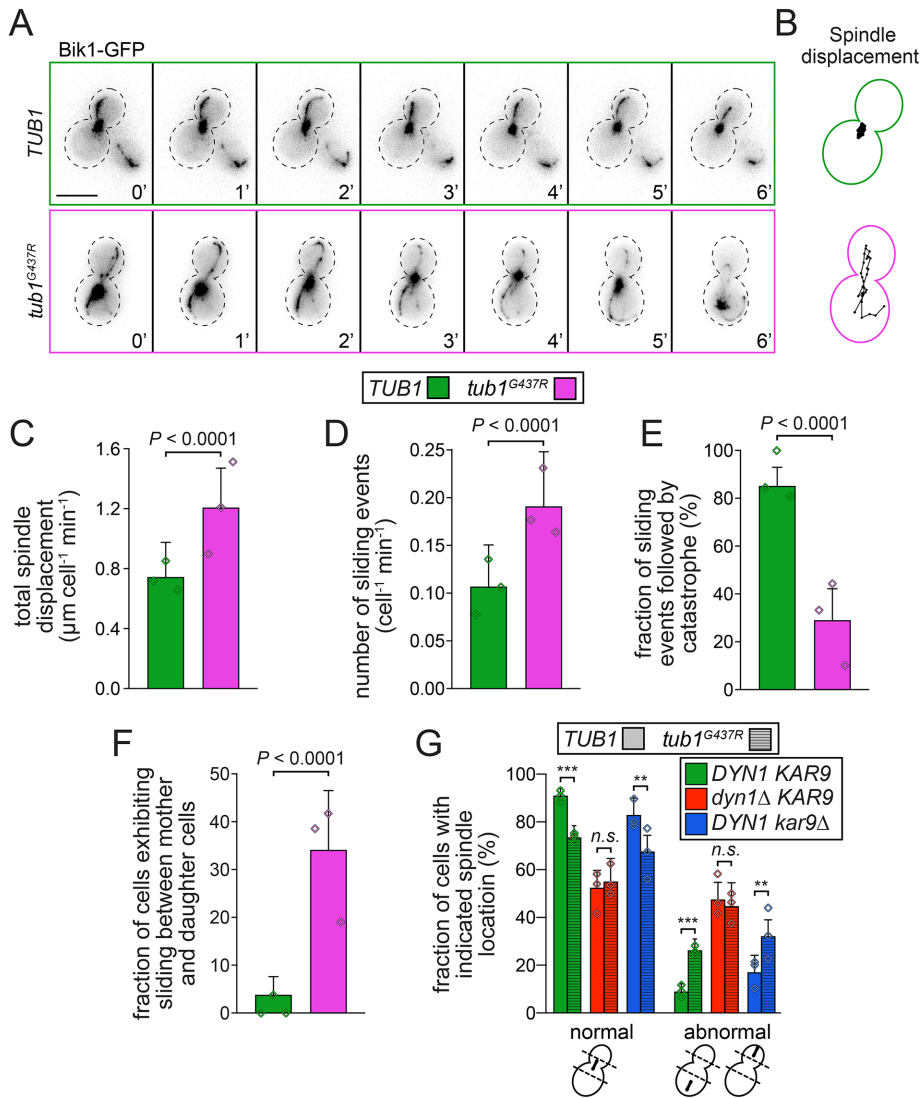


FIGURE 4: Tub1^{G437R} leads to enhanced spindle dynamics and a spindle mispositioning phenotype. (A) Representative inverse fluorescence time-lapse images of wild-type (*TUB1*) and *tub1*^{G437R} mutant cells expressing Bik1-GFP. Note the increased spindle movements that are coincident with microtubule sliding events in the mutant cell (bottom; see 3'–6' in the *tub1*^{G437R} mutant example for a typical sliding event). Scale bar, 5 μm . (B) Displacement traces of the spindle noted over the 10 min acquisition period (each spot represents the position of the spindle centroid over time). (C, D) Plots depicting the average total displacement of the mitotic spindles in wild-type or mutant cells per minute of the acquisition period (C; $n = 74$ and 52 cells from three independent clones for *TUB1* and *tub1*^{G437R} strains, respectively) or the number of microtubule sliding events (in which a microtubule appears to slide along the cell cortex) per cell per minute (D; $n = 57$ and 41 cells from three independent clones for *TUB1* and *tub1*^{G437R} strains, respectively). Bars represent mean values with SE. (E) Fraction of microtubule sliding events (described above) that are followed by a microtubule catastrophe ($n = 40$ and 31 cells from three independent clones for *TUB1* and *tub1*^{G437R} strains, respectively). Bars represent weighted means with weighted SE of proportion. (F) Fraction of cells exhibiting microtubule sliding events in which a very long microtubule (extending from one cell compartment to the other) slides over the bud and mother cell before terminating ($n = 57$ and 46 cells from three independent clones for *TUB1* and *tub1*^{G437R} strains, respectively). Bars represent weighted means with weighted SE of proportion. (G) Plot depicting the fraction of cells with the indicated spindle location in control and mutant cells (from left to right, $n = 233, 255, 141, 78, 82,$ and 130 cells from three independent clones). Bars represent weighted means with weighted SE of proportion. Statistical tests revealed $P < 0.0001$ for *TUB1* versus *tub1*^{G437R} (***), $P = 0.7069$ for *TUB1 dyn1* Δ versus *tub1*^{G437R} *dyn1* Δ and $P = 0.0143$ for *TUB1 kar9* Δ versus *tub1*^{G437R} *kar9* Δ cells. For all panels, G2/M cells (determined based on morphological criteria, i.e., those with a bud diameter $\geq 75\%$ of the mother cell) were selected for analysis. For panels C and D, P values were calculated using an unpaired Welch's t test; for panels E–G, statistical significance was determined by

previously described (Winey et al., 1995; O'Toole et al., 1999, 2002). This revealed that spindles in the mutant cells were morphologically indistinct from those in wild-type cells (Figure 3G and Supplemental Videos S1 and S2). Specifically, the number of microtubules per mitotic spindle in the mutant cells (34 ± 1.7 , mean \pm SD, for *tub1*^{G437R}) was similar to those values observed in our wild-type cells (40.5 ± 4.9 , mean \pm SD, for *TUB1*) and to those measured previously (between 26 and 62 microtubules per spindle [Winey et al., 1995; Nazarova et al., 2013; Fees et al., 2016; Leary et al., 2019]). To confirm this result, we compared the spindle-localized fluorescence intensity values for GFP-Bim1 (homologue of human EB1) in wild-type and *tub1*^{G437R} cells, a protein that binds to microtubule plus ends and localizes prominently to the spindle midzone (Schwartz et al., 1997; Khmelinskii et al., 2007; Gardner et al., 2008; Zimniak et al., 2009). This revealed no significant difference in the intensity values for Bim1 spindle localization between wild-type and *tub1*^{G437R} cells (Supplemental Figure S4, A and B). Thus, although our tomogram data set was small, our data suggest that neither the mutation nor the increased incorporation of Tub3 into the spindle microtubules leads to alterations in spindle microtubule number or defects in spindle assembly. It is interesting to note that the total number and length of microtubules appear to be unchanged in the mutant cells despite the significant reduction in total α -tubulin levels. This suggests that the levels of α -tubulin in *tub1*^{G437R} cells (and likely *tub3* Δ as well) remain above the critical concentration required for microtubule assembly. This is consistent with a previous study indicating that cells with α -tubulin levels reduced by as much as 50% are phenotypically normal (Katz et al., 1990).

The G437R mutation leads to increased spindle dynamics and impaired spindle positioning

Because the G437R mutation specifically affects microtubule dynamics during G2/M, during which astral microtubules facilitate mitotic spindle movements (by the Kar9/actomyosin and dynein pathways), we sought to assess the consequence of the mutation on these movements using Bik1-GFP as a fluorescent reporter (Figure 4A).

calculating Z scores as previously described (Marzo et al., 2019). For all plots, diamonds represent mean values obtained from each independent replicate experiment.

In wild-type cells, spindles sample a relatively small area near the bud neck in the mother cell, and most of them are oriented along the mother–bud axis (Supplemental Figure S4, B and C). Although the majority of spindles in *tub1^{G437R}* cells were also oriented along the mother–bud axis (Supplemental Figure S4C), they exhibited highly dynamic behavior; specifically, we observed numerous instances of the spindle oscillating back and forth between the mother and daughter cell compartments (Figure 4, A and B, bottom). To quantitate this phenomenon, we measured the total distance over which the mitotic spindle moves per minute within each cell. Compared with wild-type cells (*TUB1*), spindles in *tub1^{G437R}* cells move a significantly longer distance (0.7 vs. 1.2 $\mu\text{m cell}^{-1} \text{min}^{-1}$; Figure 4C). These observations indicate that excessive forces originating from the mother and bud cortex are exerted upon the mitotic spindle in *tub1^{G437R}* cells. We also noted that the spindle movements in *tub1^{G437R}* cells occur coincidentally with microtubule “sliding” events, during which the plus end of the astral microtubule contacts the cell cortex and then curls along it, all the while maintaining lateral contact (see Figures 4A, bottom, and 3’–6’; Supplemental Video S3). Quantitation of these movements—which are characteristic of dynein-mediated spindle movement events (Adames and Cooper, 2000)—revealed an approximately twofold increase in their frequency in *tub1^{G437R}* cells with respect to wild-type cells (Figure 4D).

A recent study found that dynein-mediated microtubule sliding events are often followed by a microtubule catastrophe (also mediated by dynein), which plays a role in attenuating the spindle movement events (Estrem *et al.*, 2017). We noted that these particular microtubule catastrophe events (i.e., those following sliding events) are greatly reduced in *tub1^{G437R}* cells (29% of sliding events are followed by catastrophe in *tub1^{G437R}* cells vs. 85% in wild-type cells; Figure 4E), suggesting that the G437R mutation reduces dynein’s ability to promote a catastrophe. Also consistent with these data, a larger fraction of mutant cells appeared to exhibit events in which very long microtubules that extended from one compartment to the other (i.e., mother to bud or vice versa) underwent characteristic dynein-mediated sliding between the two cellular compartments (Figure 4F; also see Supplemental Video S3).

The main function of cytoplasmic microtubules in vegetative yeast cells is to orient the mitotic spindle along the mother–bud axis (presumably by the Kar9/actomyosin pathway) and localize it proximally to the bud neck (by the dynein pathway) such that at the time of anaphase onset, the chromosomes are divided equally between the mother and daughter cells (Li *et al.*, 1993; Carminati and Stearns, 1997; Yin *et al.*, 2000; Hwang *et al.*, 2003; Liakopoulos *et al.*, 2003). Although we found that orientation of the spindle along the mother–bud axis was not compromised in *tub1^{G437R}* cells (Supplemental Figure S4; note that our data suggest that both dynein and Kar9/actomyosin pathways affect this phenomenon), we did note that the spindle was more frequently localized to the apical regions of the mother or daughter cells in the *tub1^{G437R}* strain (26% of *tub1^{G437R}* cells vs. 9% of wild-type cells; Figure 4G). Analysis of cells deleted for either the dynein heavy chain (*DYN1*) or *KAR9* with or without *tub1^{G437R}* revealed that the tubulin mutation increases the frequency of spindle-position defects in *kar9 Δ* but not *dyn1 Δ* cells, suggesting that G437R disrupts the function of the dynein but not the Kar9/actomyosin pathway (Figure 4G). Taken together, these observations suggest that the G437R mutation leads to increased dynein-mediated spindle movements and yet reduced dynein-mediated microtubule catastrophe events (following sliding events), which ultimately leads to a spindle-mispositioning phenotype.

Enhanced spindle dynamics in *tub1^{G437R}* mutant cells are dynein dependent

As noted above, the dynein pathway mediates microtubule sliding events that result in translocation of the mitotic spindle throughout the cell. Given our observations noted above, we sought to determine whether the *tub1^{G437R}* mutant phenotypes are a consequence of hyperactive dynein. Consistent with the notion that dynein is responsible for the observed spindle behavior in *tub1^{G437R}* cells, the increased spindle displacement phenotype in *tub1^{G437R}* cells was eliminated by deletion of *DYN1* but not by deletion of *KIP3*, a kinesin that has been implicated in regulating microtubule length and spindle movements (Figure 5, A and B) (Gupta *et al.*, 2006; Fukuda *et al.*, 2014).

We next asked whether the increased dynein activity is due to enhanced targeting of dynein to microtubule plus ends or the cell cortex, which can be causative of increased cellular dynein activity (Markus *et al.*, 2011). To this end, we imaged Dyn1-3GFP in cells also expressing RFP-Tub1 (or RFP-Tub1^{G437R}) in wild-type or *tub1^{G437R}* cells (Figure 5, C–E). We found no significant difference in either the frequency of Dyn1-3GFP targeting or the fluorescence intensity values for Dyn1-3GFP at microtubule plus ends, SPBs, or the cell cortex (Figure 5, D and E). Thus, the increased dynein activity in *tub1^{G437R}* cells is likely not a consequence of increased localization to any of these sites.

G437R tubulin and microtubules exhibit reduced interaction with the dynein regulator She1

We wondered whether the apparent increase in dynein activity in *tub1^{G437R}* cells could be a consequence of reduced microtubule binding by the MAP She1, a dynein inhibitor (Woodruff *et al.*, 2009; Markus *et al.*, 2011, 2012). To determine whether this might be the case, we first employed our spindle dynamics assay, which revealed that deletion of She1 in otherwise wild-type cells leads to an increase in spindle displacement (Figure 5A). Interestingly, the extent of the increase was similar to that noted in *tub1^{G437R}* cells and was only mildly increased further by the addition of the *tub1^{G437R}* allele. Thus, the *tub1^{G437R}*-dependent increase in spindle displacement is phenocopied by and partially epistatic to *SHE1* deletion.

We previously found that She1-mediated inhibition of dynein activity requires its microtubule-binding activity (Ecklund *et al.*, 2017). To determine whether G437R affects the She1–microtubule interaction, we employed several approaches. First, we tested the effect of G437R on the interaction between She1 and tubulin. A She1-Gal4 activation domain (AD) fusion was tested for a two-hybrid interaction with either Tub1 or Tub1^{G437R}, the latter of which was fused to the LexA DNA-binding domain (LexA_{DBD}). Bim1, which is known to interact with α -tubulin in a two-hybrid assay (Schwartz *et al.*, 1997; Krogan *et al.*, 2006), was used as positive control, as was the kinesin Kip3. As expected, Bim1, Kip3, and She1 all exhibited a two-hybrid interaction with the Tub1 bait (Figure 6A; positive interactions are apparent by growth on media lacking histidine, “–HIS”). Interestingly, the interaction between She1 and Tub1—but not between Tub1 and either Bim1 or Kip3—was reduced to background levels by the G437R mutation (Figure 6A).

Like many MAPs, the interaction between She1 and microtubules requires the disordered C-terminal tails of tubulin (Markus *et al.*, 2012; Ecklund *et al.*, 2017). Thus, to further confirm the importance of G437 in the She1-tubulin interaction, we performed a pull-down assay in which this interaction was competitively inhibited by the addition of a peptide encompassing the C-terminus of Tub1 (amino acids 415–447; both She1 and tubulin were used at 5 $\mu\text{g}/\text{ml}$ or below, well below the critical concentration required for microtubule

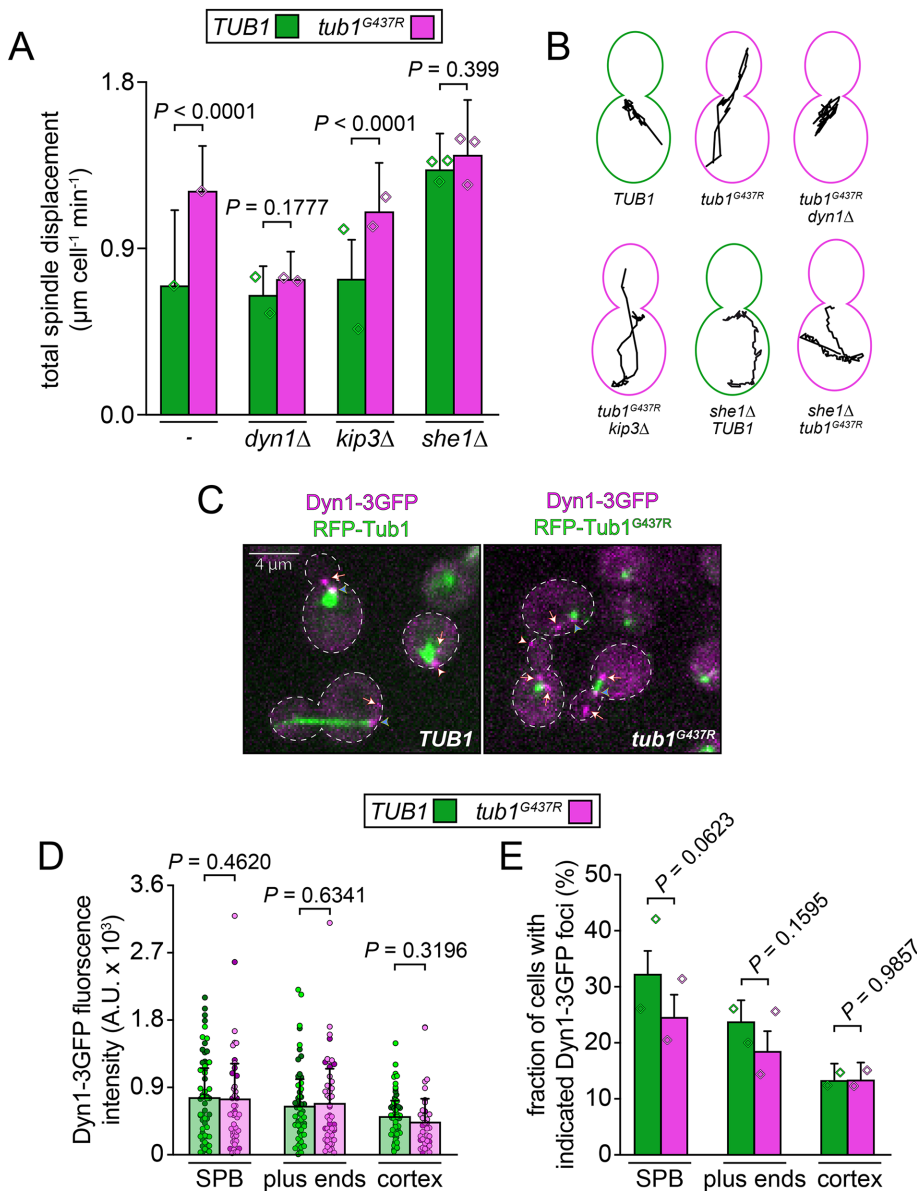


FIGURE 5: Enhanced spindle movement phenotype in *tub1^{G437R}* cells is dynein dependent. (A) Plot depicting the average total displacement of the mitotic spindle in cells with the indicated genotype per minute of the acquisition period (for strains from left to right, $n = 63, 24, 35, 35, 55, 35, 45,$ and 45 cells from two or three independent clones, respectively; P values were calculated using an unpaired Welch's t test). (B) Representative displacement traces of the spindle noted over the 10 min acquisition duration for the indicated strains. (C) Representative fluorescence images of cells expressing Dyn1-3GFP and RFP-Tub1 (wild type or mutant) in either wild-type or mutant cells, as indicated (white arrowheads indicate cortical foci, the white arrows indicate plus end foci, and the blue arrowheads indicate SPB foci). (D, E) Fluorescence intensity measurements of (D) and fraction of cells with (E) Dyn1-3GFP foci at the indicated subcellular localization in *TUB1* and *tub1^{G437R}* strains (for D, data sets from left to right, $n = 56, 52, 58, 49, 60,$ and 36 cells from two independent replicates; values from independent replicates are shown in two shades of green and magenta; for E, $n = 248$ and 232 cells for wild-type and mutant cells, respectively, from two independent replicates). For panel A, P values were calculated using an unpaired Welch's t test. Diamonds represent mean values obtained from each independent replicate experiment.

assembly). To this end, a 6His-She1 C-terminal fragment (She1^{Cterm}; residues 194–338; which is sufficient for microtubule binding [Zhu et al., 2017]) was incubated with tubulin (see Figure 6B for specificity of tubulin–She1^{Cterm} interaction) in the absence or presence of a pep-

tide corresponding to the C-terminus of either wild-type or G437R tubulin. The relative extent to which the NiNTA bead-immobilized 6His-She1^{Cterm} pulled down tubulin was subsequently assessed by SDS–PAGE and immunoblot (using an antibody against α -tubulin). This revealed that the She1^{Cterm}–tubulin interaction was strongly competed by the wild-type peptide, but much less so by the same peptide with the G437R mutation (Figure 6C).

In an attempt to directly measure the ability of She1 to bind to microtubules composed of Tub1^{G437R} and Tub2 (the latter encoding β -tubulin), we purified wild-type and mutant tubulin heterodimers from budding yeast using previously established methodologies (Gupta et al., 2001; Johnson et al., 2011) (in which Tub2 is fused to a C-terminal 6His tag; Supplemental Figure S5A). We confirmed the presence of Tub1, Tub2 (both of which were overexpressed), and low levels of copurifying Tub3 (which was not overexpressed) in both protein preparations by liquid chromatography–coupled tandem mass spectrometry (LC/MS) (Supplemental Figure S5B). These data also revealed that similar amounts of wild-type and mutant Tub1 copurified with Tub2, indicating that each is equally competent for heterodimerizing with Tub2. However, although we were able to reconstitute yeast microtubules using purified wild-type Tub1/Tub2 heterodimers (Supplemental Figure S5C), we were unable to do so using purified Tub1^{G437R}/Tub2. The inability of the mutant protein to polymerize suggests that Tub1^{G437R} is not sufficient to assemble microtubules in the absence of Tub3 (as suggested by the synthetic lethality of *tub1^{G437R}* and *tub3 Δ*) and the mutation functionally compromises tubulin's polymerization activity.

We thus employed an alternate strategy to assemble microtubules from either wild-type or mutant tubulin (Bergman et al., 2018). Specifically, we prepared concentrated cell lysates from either wild-type or *tub1^{G437R}* cells (both of which possessed wild-type *TUB3*) and incubated them in microscope chambers in which preassembled microtubule seeds were affixed. This results in the polymerization of microtubules (due to the high concentration of tubulin within the extracts; see Supplemental Figure S5D, for example) that we then incubated with recombinant, fluorescent She1 (She1-HaloTag⁶⁶⁰) purified from budding yeast. This revealed that She1 indeed binds to

wild-type microtubules to a greater extent than those prepared from *tub1^{G437R}* cells (Figure 6, D and E).

Finally, we measured the extent to which She1 localizes to microtubules in cells by comparing the relative recruitment of full-length

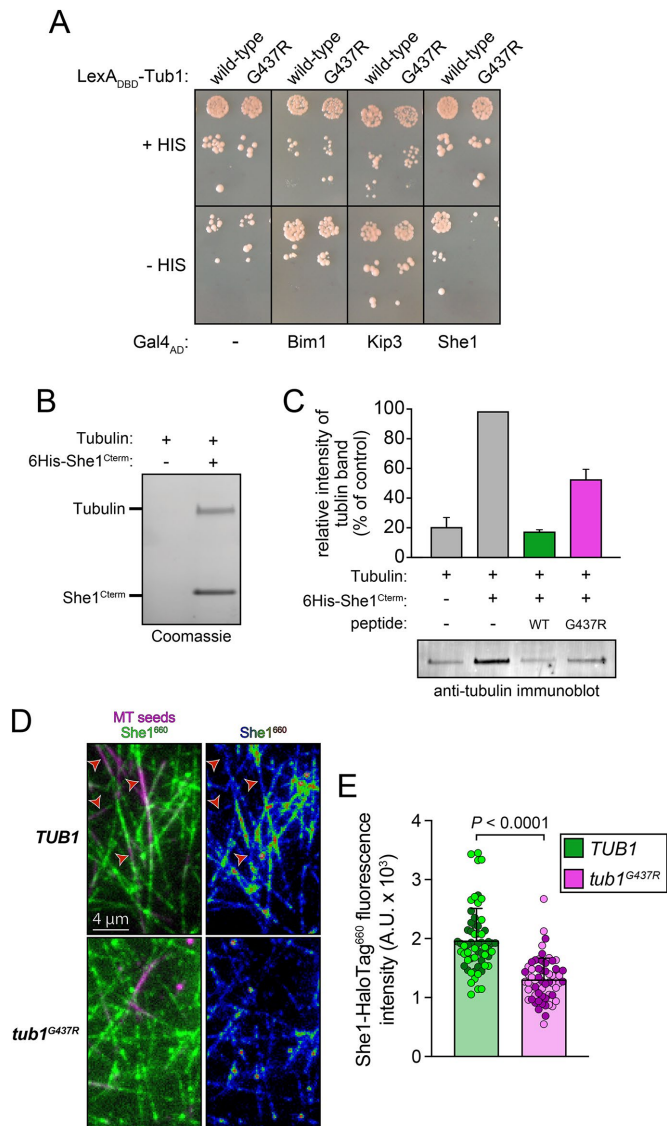


FIGURE 6: She1–tubulin and microtubule binding is reduced by the G437R mutation. (A) Two-hybrid assay illustrating the relative degree of interaction between tubulin (wild type or mutant) and either the microtubule end-binding protein Bim1 (homologue of human EB1), the kinesin-8 Kip3, or the dynein inhibitor She1. Serial dilutions of cells were spotted on minimal solid media with (top) or without (bottom) histidine. Growth on histidine-deficient media is indicative of an interaction between bait and prey proteins. (B) Coomassie-stained acrylamide gel illustrating a representative pull down of cow brain tubulin by NiNTA-immobilized 6His-She1^{Cterm}. (C) Representative anti-tubulin immunoblot and quantitation of an experiment in which a peptide corresponding to the tubulin C-terminal tail (wild type or mutant) was used to compete bound tubulin off of a NiNTA-immobilized 6His-She1^{Cterm} ($n = 2$ independent replicates). (D) Representative fluorescence images (left, along with heatmap depicting relative intensity of She1-HaloTag⁶⁶⁰, right) depicting purified She1 binding to microtubules polymerized using tubulin from yeast cells with the indicated genotype (arrowheads depict some of the microtubule seeds to which She1 appears to bind to a lower extent). (E) Plots depicting fluorescence intensity values (mean \pm SD) for microtubule-bound She1 ($n = 60$ microtubules for each condition from two independent replicates; all values from independent replicates are shown in two shades of green and magenta). The P value was calculated using a Mann–Whitney test.

She1 to spindle microtubules (where She1 fluorescence is most prominent) in either wild-type or *tub1*^{G437R} cells. Consistent with the two-hybrid and in vitro data described above, we found that spindle-localized She1 fluorescence was 55.7% lower in *tub1*^{G437R} cells than in wild-type cells (Figure 7, A and B).

As noted above, spindle microtubules in *tub1*^{G437R} cells are composed of a greater proportion of Tub3 than those in wild-type cells (see Figure 3E). Thus, the reduced microtubule-binding (Figure 6E) and She1-spindle localization (Figure 7B) noted above could potentially be a consequence of She1 binding to Tub3-containing microtubules to a lesser extent. To determine whether this might be the case, we sought to engineer yeast cells expressing only Tub3. Although the expression of one copy of *TUB3* in the absence of *TUB1* is indeed lethal, previous studies reported that this lethality could be rescued by integration of a second copy of *TUB3* into the genome (Schatz *et al.*, 1986b; Bode *et al.*, 2003). To this end, we integrated a plasmid expressing Tub3 (under control of the strong constitutive promoter *TEF1p*) into the genome of *TUB1/tub1* Δ heterozygote diploid cells, sporulated them, and assessed the viability of the recovered progeny. As expected, no single *tub1* Δ mutants were recovered, while all *tub1* Δ *TEF1p:TUB3* double mutants were indeed viable (Supplemental Figure S6A), although with colony sizes significantly smaller than those in wild type (Supplemental Figure S6B). Interestingly, we noted that *TUB1 TEF1p:TUB3* cells were less healthy than *tub1* Δ *TEF1p:TUB3* double mutants, as was apparent by the reduced colony size of the former (Supplemental Figure S6B). Although the growth defects for these cells may be a consequence of the excessive α -tubulin levels, previous studies have found that overexpressing Tub1 does not compromise cell viability (in contrast to Tub2) (Burke *et al.*, 1989).

Using the *tub1* Δ *TEF1p:TUB3* (“*TUB3*-only”) cells, we found that the extent of spindle-localized She1 was not reduced on microtubules composed of only Tub3-Tub2 heterodimers. In fact, the mean intensity of spindle-localized She1 was 61.7% greater in *TUB3*-only cells. To confirm these results and to more carefully determine the relative ability of She1 to associate with Tub1- versus Tub3-containing microtubules, we assessed the extent to which She1 binds to microtubules generated from concentrated lysates prepared from either *TUB1*-only (*TUB1 tub3* Δ) or *TUB3*-only (*TEF1p:TUB3 tub1* Δ) cells. This revealed that She1 exhibits a slight preference for microtubules composed of Tub3-Tub2 versus Tub1-Tub2 heterodimers (Figure 7, E and F). Taken together, these findings indicate that She1 indeed binds to Tub1^{G437R}-containing microtubules to a lesser extent, thus accounting for the hyperactive dynein phenotype in these cells.

Mitotic spindles in *TUB3*-only cells are comprised of more microtubules than those in wild-type cells and are misoriented

As noted above, our immunoblot and fluorescence data suggest that Tub3-Tub2 heterodimers comprise a larger fraction of cellular microtubules than previous results have suggested. In light of this, we wondered what—if any—consequences would result from eliminating all the Tub1 α -tubulin isotype from microtubules that comprise the mitotic spindle. To this end, we modeled spindle microtubules from tomographic volumes generated from our *TEF1p:TUB3 tub1* Δ (“*TUB3*-only”) mutant cells. This analysis revealed one striking difference between spindles from *TUB3*-only cells and those from wild-type cells: three of the four models from preanaphase cells (“P-A”) revealed a much larger number of microtubules emanating from each SPB (64, 74, and 76 total microtubules per mitotic spindle, respectively; Figure 8A and Supplemental Videos S4 and S5), while the fourth possessed a number much closer to wild-type

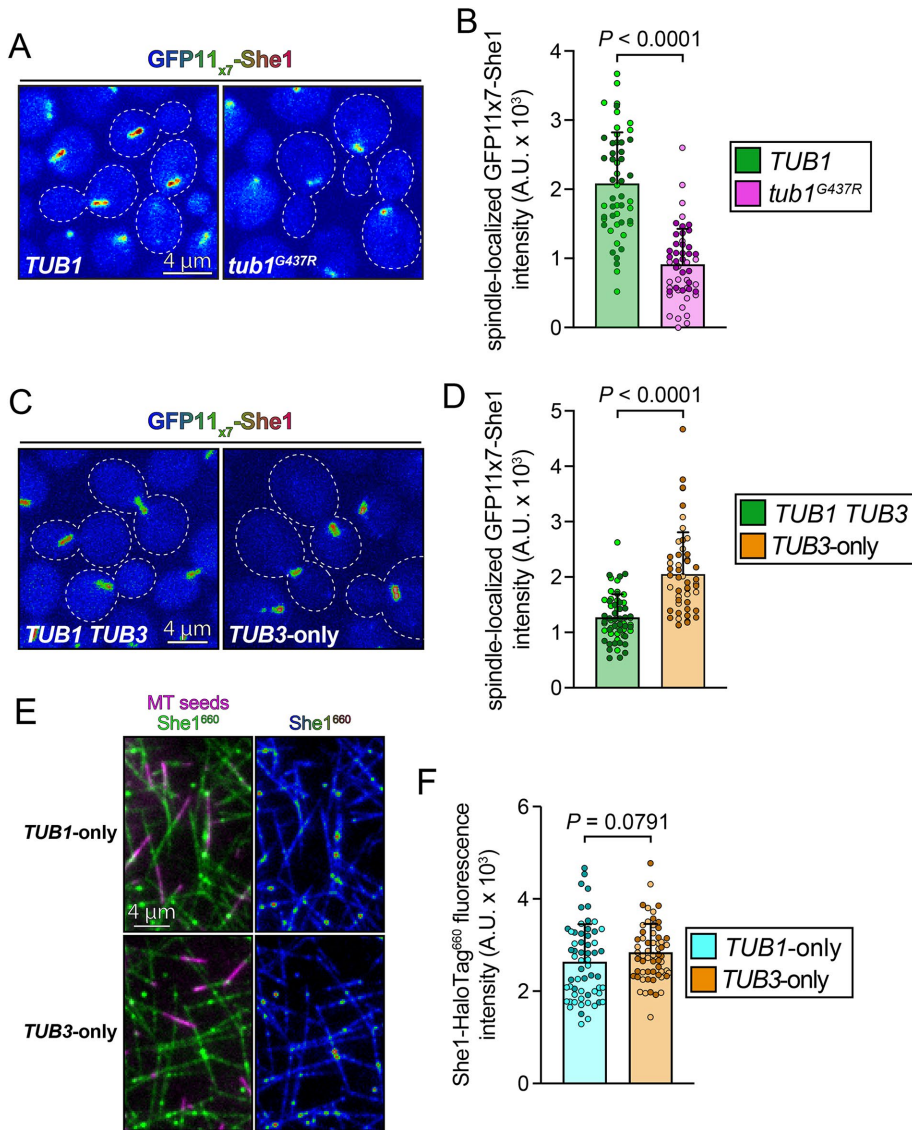


FIGURE 7: In vivo microtubule binding by She1 is reduced by the G437R mutation. (A–D) Representative fluorescence images (shown as a heatmap; A and C) and quantitation (B and D) depicting the relative degree of spindle-localized GFP_{11x7}-She1 in wild-type or mutant cells, as indicated. Before imaging, cells were arrested with 200 mM hydroxyurea (HU) for 2.5 h (to enrich for cells with mitotic spindles) and then mounted on agarose pads containing HU for fluorescence microscopy ($n = 52$ cells for each condition for B and $n = 60$ and 53 cells for TUB1 TUB3 and TUB3-only cells, respectively, for C, all from two independent replicates; all values from independent replicates are shown in two shades of green, magenta, or orange, along with mean \pm SD). P values were calculated using an unpaired Welch’s t test. (E) Representative fluorescence images (left, along with heatmap depicting relative intensity of She1-HaloTag⁶⁶⁰, right) depicting purified She1-HaloTag⁶⁶⁰ binding to microtubules polymerized using tubulin from yeast cells with the indicated genotype. (F) Plots depicting fluorescence intensity values (mean \pm SD) for microtubule-bound She1 ($n = 60$ microtubules for each condition from two independent replicates; all values from independent replicates are shown in two shades of blue and orange). The P value was calculated using a Mann–Whitney test. (G) Model of spindle microtubules built from EM tomographic volumes from a preanaphase TUB3-only cell, along with the parameters determined. Green and magenta lines depict microtubules emanating from SPB1 and SPB2, respectively, and blue disks depict SPBs (“P-A” and “M-A” indicate cells that are in preanaphase and midanaphase, respectively).

values (38 total). Measurements of SPB diameters revealed that those cells with larger numbers of microtubules also possessed larger SPBs (Figure 8A). These findings suggest that the increased spindle intensity values for She1 in TUB3-only cells may largely be a

consequence of the increased microtubule number, especially in light of the small increase in She1-binding affinity for Tub3-only microtubules that we observed in vitro.

We next assessed whether spindles from TUB3-only cells can assemble a “core bundle” of microtubules—antiparallel microtubules emanating from opposite spindle poles that laterally associate and likely participate in spindle elongation during anaphase (Winey et al., 1995). This revealed that a core bundle was indeed present in longer spindles (e.g., in cell numbers 1, 3, and 4), including one spindle that was in the midst of anaphase (cell number 5). These observations suggest that microtubule cross-linking proteins (e.g., Ase1, Kip1, Cin8) are capable of binding to microtubules composed entirely of Tub3-Tub2 heterodimers.

Much like our TUB3-only cells, a previous study found that spindles from mitotically arrested cells (using a conditional mutant of the checkpoint protein Cdc20) possess greater numbers of microtubules emanating from each SPB (mean of 81 microtubules per spindle) (O’Toole et al., 1997). Thus, we wondered whether the increased microtubule number in the TUB3-only cells is a consequence of a mitotic arrest phenotype. To determine whether this may be the case, we quantitated mitotic duration by measuring the interval of time between SPB duplication (a marker for the start of spindle assembly) and onset of anaphase (as determined by the separation of the SPBs from one another). This revealed a 26% delay between the initiation of spindle assembly and anaphase onset (Figure 8B), indicating that a mitotic arrest may possibly account for the expansion of the SPB noted by our EM analysis. However, compared with the extensive arrest employed with the *cdc20-1* mutant cells described above (grown for 4 h at the restrictive temperature) (O’Toole et al., 1997), it is unclear whether this short delay (39.9 vs. 50.3 min) is the basis for the expanded SPB and enhanced microtubule number in these cells.

In addition to increased microtubule numbers in TUB3-only cells, we also noted the presence of preanaphase spindles in these cells that were not oriented along the mother–bud axis (e.g., see Supplemental Video S4). We quantitated this phenomenon by measuring the angle of the mitotic spindle with respect to the mother–bud axis (Figure 8C), which revealed that TUB3-

only cells indeed exhibit a spindle orientation defect similar to that of cells deleted of either *KAR9* or *DYN1* (see Supplemental Figure S4, B and C). In contrast, we noted that spindles in the TUB3-only cells were not mislocalized to the apical regions of the mother or

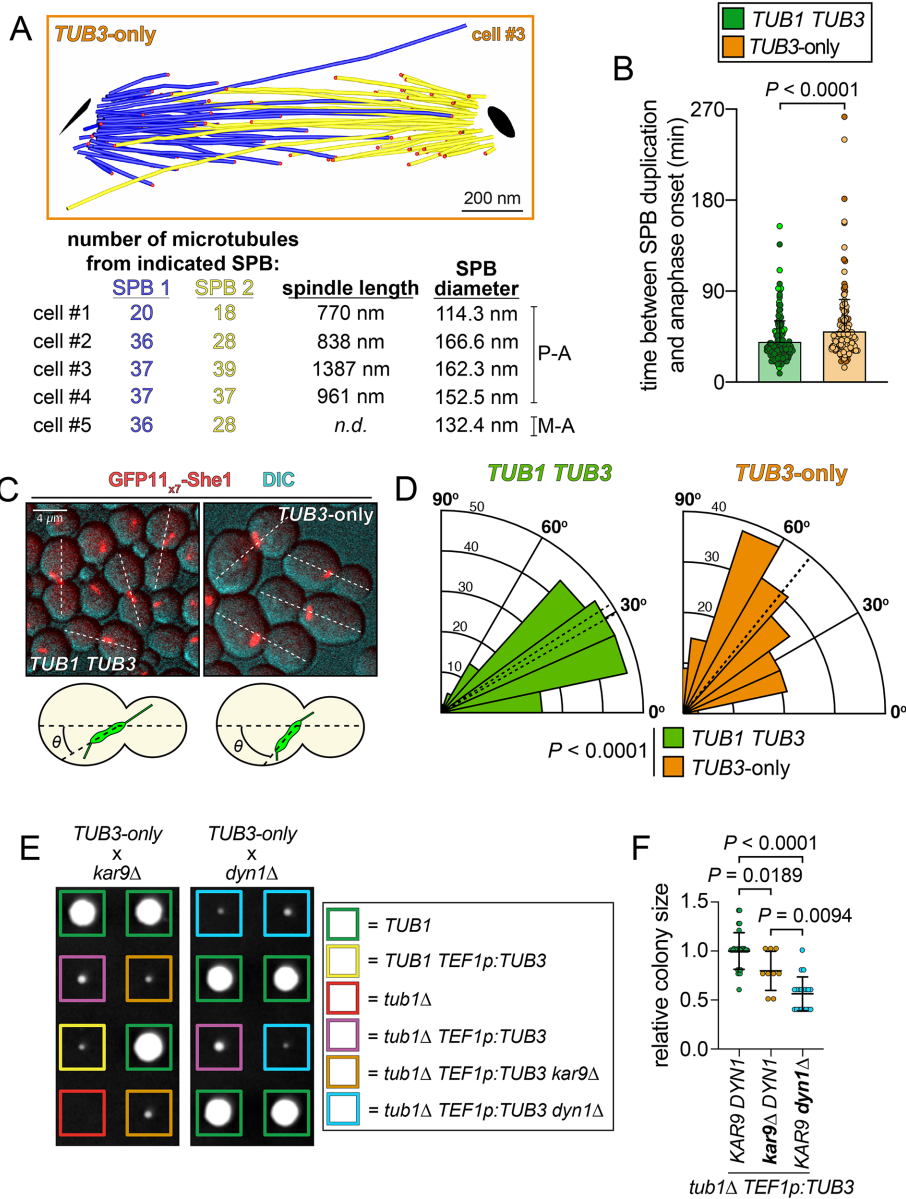


FIGURE 8: *TUB3*-only cells nucleate more spindle microtubules from enlarged SPBs. (A) Model of spindle microtubules built from EM tomographic volumes from a preanaphase *TEF1p:TUB3 tub1Δ* (“*TUB3*-only”) cell, along with parameters determined from five models. Blue and yellow lines depict microtubules emanating from SPB1 and SPB2, respectively, red spheres depict microtubule plus ends, and black disks depict SPBs (scale bar, 200 nm; “P-A” and “M-A” indicate cells that are in preanaphase and midanaphase, respectively). (B) Plot depicting time interval between SPB duplication (a marker for the initiation of spindle assembly) and anaphase onset ($n = 197$ and 196 cells for wild-type and *TUB3*-only cells, respectively, from two independent replicates each). Cells were grown in a microfluidics cassette (CellASIC ONIX; see *Materials and Methods*) and imaged over the course of several cell cycles. The P value was calculated using a Mann–Whitney test. (C) Representative images and cartoon schematic depicting spindle angles measured and plotted in panel D (dashed lines indicate mother–bud axis in select cells; note that drawings indicate mean spindle angle for wild-type and mutant cells). Before imaging, cells were arrested with 200 mM HU for 2.5 h (to enrich for cells with mitotic spindles) and then mounted on agarose pads containing HU for fluorescence microscopy. (D) Rose plots depicting the angles of preanaphase spindles with respect to the mother–bud axis ($n = 186$ and 165 cells from two independent replicates from *TUB1 TUB3* and *TUB3*-only cells, respectively). Dashed lines indicate mean values for independent replicates (32.6° and 30.6° for *TUB1 TUB3* and 51.0° and 50.8° for *TUB3*-only). The P value was calculated using a Mann–Whitney test. (E) Representative images of colonies (grown on YPAD) from a tetrad dissection from mating *TUB3*-only (*tub1Δ TEF1p:TUB3*) cells with either *kar9Δ* (left) or *dyn1Δ* (right) mutants depicting the relative size of *TUB3*-only *kar9Δ* (orange boxes), *TUB3*-only *dyn1Δ* (light blue boxes)

daughter cells (Supplemental Figure S6C; compare to Figure 4G), suggesting that dynein function is not compromised in cells containing microtubules exclusively composed of Tub3-Tub2 heterodimers. These data also confirm that the increased incorporation of Tub3 into microtubules in *tub1^{G437R}* cells is not responsible for the spindle-positioning defect in these cells, and in fact the presence of Tub1^{G437R} appears to protect cells against defects in spindle orientation.

Finally, in an attempt to determine whether *TUB3*-only cells are compromised in dynein or Kar9 function, we mated them with either *dyn1Δ* or *kar9Δ* cells and assessed the viability of the resulting haploid *TUB3*-only *kar9Δ* or *TUB3*-only *dyn1Δ* mutant cells. It is well established that budding yeast rely on dynein or Kar9 pathway function for viability and that defects in either pathway result in synthetic growth defects when combined with mutations in the other (Miller and Rose, 1998). Although all triple mutants (*tub1Δ TEF1p:TUB3 dyn1Δ* and *tub1Δ TEF1p:TUB3 kar9Δ*) were viable, we noted that their respective colony sizes were smaller than those with wild-type *KAR9* and *DYN1* (Figure 8E). Colony area measurements revealed that *TUB3*-only *dyn1Δ* cells exhibited more-severe growth defects than *TUB3*-only *kar9Δ* cells (Figure 8F). Although additional study is required to definitively determine which pathway is compromised in *TUB3*-only cells, these data suggest that *KAR9* pathway function is more significantly impacted than dynein pathway function. These data suggest that Tub1 and Tub3 have unique, noncomplementary functions that are each required for microtubule-dependent functions. Although the mechanism underlying disruption of the Kar9 pathway in *TUB3*-only cells is unclear, it may be a consequence of disrupted microtubule binding by effectors of this pathway (e.g., Bim1, Kip3).

DISCUSSION

In summary, we have used budding yeast to characterize the consequences of mutating

colonies, and *TUB3*-only (purple boxes) colonies. Two representative tetrads are shown from each. (F) Plot depicting relative area of colonies with the indicated genotype. Note that the combination of *TUB3*-only with *dyn1Δ* results in smaller colony sizes than either *TUB3*-only *kar9Δ* or *TUB3*-only alone (from left to right, $n = 30$, 9, and 19 mutants obtained from 47 and 63 tetrads from each dissection, respectively). P values were calculated using an unpaired Welch’s t test.

G437 in α -tubulin (equivalent to G436 in TUBA1A), which was likely causative of MCD in at least two human patients (Bahi-Buisson *et al.*, 2008; Hebebrand *et al.*, 2019). Our results indicate that the mutant protein retains the ability to assemble into microtubules; however, we find that it is incorporated into microtubules to a lesser extent than wild-type α -tubulin due to either protein degradation or structural and/or functional defects associated with the mutation. Our inability to generate microtubules in vitro using only purified Tub1^{G437R} and Tub2 suggests that the latter is more likely. The reduced incorporation of the mutant tubulin into microtubules appears to be compensated by a corresponding increase in Tub3 incorporation in the tub1^{G437R} mutant cell microtubules. Although the mutant cells are capable of assembling mitotic spindles that are morphologically indistinct from those of wild-type cells, they exhibit dramatic alterations in their spindle positioning function. Using a combination of in vitro and in vivo methods, we attribute these changes to hyperactive dynein function that is likely a direct consequence of reduced microtubule binding by the dynein inhibitor She1. Moreover, the disrupted She1–microtubule binding in these cells is a direct consequence of microtubule-incorporated Tub1^{G437R} and not increased Tub3 levels. These data are consistent with our recent findings that She1 must bind to microtubules to inhibit dynein motility (Ecklund *et al.*, 2017).

We find that Tub1^{G437R}-Tub2 heterodimers occupy only a small fraction of microtubules in cells (17–22%), with Tub3-Tub2 comprising the majority. Despite this, the mutant appears to reduce the She1–microtubule interaction by 56.1% in cells and 33.6% in vitro, suggesting that Tub1^{G437R}-Tub2 heterodimers are reducing the ability of neighboring Tub3-Tub2 heterodimers to bind She1. Although a cooperative microtubule-binding mechanism by She1 may potentially account for this, no such cooperativity has been observed (Markus *et al.*, 2012). Thus, in addition to directly affecting individual MAP-binding sites (i.e., in direct proximity of G437), these data suggest that the mutation exerts allosteric effects on the overall surface architecture of the microtubule. Previous evidence indicates that allostery can indeed be propagated along the lattice. For example, binding of kinesin-1 at its intradimer binding site on the microtubule has been shown to allosterically affect microtubule structure, which in turn promotes the binding of additional kinesins to neighboring binding sites (Shima *et al.*, 2018). This model can account for how tubulin mutants that retain polymerization activity can “poison the well” and exert dominant negative effects on cellular microtubule function, whereas those heterozygous tubulin mutations that lead to protein misfolding or polymerization incompetence are more likely to be innocuous.

It is interesting to note that the effects of G437R on microtubule dynamics were significant only during the G2/M phase of the cell cycle, at which point the growth and shrinkage rates and the overall dynamicity increase significantly as a consequence of the mutation. Although the reasons for the cell cycle–dependent differences are unclear, they may be due to an inability (or an increased ability) of a G2/M-specific factor to bind to and affect microtubule dynamics (either from the plus end or along the lattice). Given the importance of the C-terminal tail in microtubule binding by numerous factors and the proximity of G437 to the C-terminal tail of α -tubulin, the possibility that this mutation is in fact impacting the structure/function of this region is a likely scenario. Although it is unclear whether She1 affects microtubule dynamics, its reduced binding affinity for the mutant microtubules raises the possibility that the altered dynamics are a direct consequence of disrupted She1–microtubule binding or an indirect cause of She1’s inability to modulate dynein or dynein–dynactin (see below). Of note, a previous study observed an ~17% increase in the

rate of microtubule polymerization in mutant α -tubulin–expressing yeast that was eliminated upon deletion of Tub3 (Gartz Hanson *et al.*, 2016), suggesting that increased incorporation of Tub3 into microtubules leads to faster polymerization rates. This observation suggests that the increased proportion of Tub3 in the microtubules in tub1^{G437R} cells may be at least partially responsible for the altered dynamicity observed here (16% increase in polymerization rate).

Also of interest is the apparent change in microtubule dynamics that we observed specifically during and subsequent to dynein-mediated microtubule sliding events. This decreased frequency of catastrophe events results in a greater proportion of long microtubules in the tub1^{G437R} strain, which may also partly account for the increase in dynein activity. It has been shown that increased microtubule lengths directly correlate with enhanced dynein activity in cells (Estrem *et al.*, 2017). Although the role of She1 in affecting microtubule dynamics is not clear, it is possible that dynein-mediated depolymerizing activity—as has been noted in vivo (Estrem *et al.*, 2017)—requires microtubule-bound She1. In particular, Estrem *et al.* (2017) recently showed that microtubules undergo a catastrophe event coincident with a dynein-mediated sliding event. They proposed that offloading of dynein–dynactin (the latter of which is a critical regulator of dynein activity) from microtubule plus ends to the cell cortex shifts the balance such that dynactin—which presumably stabilizes microtubules—is depleted from plus ends, while sufficient levels of dynein—which destabilizes microtubules—remain plus end associated. In addition, previous studies found that She1 plays a role in precluding dynein–dynactin interaction at microtubule plus ends (Woodruff *et al.*, 2009; Markus *et al.*, 2011). Thus, either dynein-mediated microtubule destabilization or dynactin-mediated microtubule stabilization might be enhanced or reduced, respectively, by microtubule-bound She1. Although it is unclear whether She1 needs to bind microtubules to affect dynein–dynactin interaction, it is possible that the Tub1^{G437R}-mediated reduction in She1–microtubule binding might also enhance dynein-mediated recruitment of dynactin to plus ends, which would presumably provide a microtubule stabilization effect (due to the increased presence of dynactin). These models are not mutually exclusive and may in fact both be acting to affect microtubule length during dynein-mediated spindle movement events.

Our findings also challenge the notion that Tub3 is a minor α -tubulin isotype in yeast. Rather, our immunoblotting and live cell imaging data indicate that Tub3 comprises approximately 50% of the free and polymerized α -tubulin pool. Despite this, yeast cells can tolerate expressing only Tub1 but are inviable when only one copy of Tub3 is expressed (Schatz *et al.*, 1986b). Although overexpressing Tub3 can compensate for this inviability (Bode *et al.*, 2003)—with significant consequences to cell health—this leads to cells with larger SPBs, greater numbers of spindle microtubules, and defects in spindle orientation. The reason for these phenotypes is unclear; however, perhaps the increase in spindle microtubule numbers is a compensatory mechanism exercised by TUB3-only cells to perform basic microtubule-dependent functions. For instance, perhaps Tub3-only microtubules bind to kinetochore-associated microtubule-binding proteins (e.g., the Ndc80 or Dam1 complexes) with lower affinity and a greater number of microtubules are required to overcome this deficit and ensure that kinetochores are captured with appropriate timing. Given the smaller C-terminal E-hook on Tub3 (only two glutamates in Tub3 vs. 4 in Tub1; see Figure 1) and the importance of this region for Ndc80 and Dam1 complex–microtubule binding (Westermann *et al.*, 2005; Ciferri *et al.*, 2008), this may be the case. This notion is supported by the somewhat prolonged interval between the initiation of spindle assembly and anaphase onset in TUB3-only cells. It is also interesting to note that the

mutant Tub1^{G437R} reduces the defects apparent in *TUB3*-only cells (compare Figure 3G to Figure 8A, and Supplemental Figure S4C to Figure 8D), indicating that even low levels of the mutant protein support microtubule functions not provided by Tub3.

Given the consequences for apparent brain development in two patients with missense mutations at TUBA1A^{G436} (pachygyria and severe microcephaly associated with postural delay and poor communication abilities in one patient, and abnormal cortical gyration among other phenotypes in a second [Bahi-Buisson et al., 2008; Hebebrand et al., 2019]) and the strong link between mutations in dynein activity and motor neuron diseases and developmental brain disorders (Vissers et al., 2010; Willemsen et al., 2012; Bahi-Buisson et al., 2014; Laquerriere et al., 2017; Marzo et al., 2019), our data linking disrupted dynein activity with this mutation are not entirely surprising. For example, dynein activity is critical for various aspects of early neuronal development, in part by promoting interkinetic nuclear migration in neuronal progenitors, and in the subsequent migration of the resulting postmitotic neurons (Del Bene et al., 2008; Tsai et al., 2010; Hu et al., 2013; Markus et al., 2020). Moreover, by mediating retrograde transport in neurons throughout their developmental progression, dynein is crucial for the maintenance of neuronal health, especially in motor neurons in which cargoes must be transported over very long distances (≤ 1 m) (Bowman et al., 2000; Shah et al., 2000; Wagner et al., 2004; He et al., 2005; Hendricks et al., 2010; Fu and Holzbaur, 2013; Rao et al., 2017). However, of note, our findings suggest that dynein itself is unaffected by the mutation; rather, dynein activity is indirectly affected by the reduced microtubule-binding affinity of a key regulatory MAP, She1. To date, a clear functional homologue of She1 in humans has not been identified. However, there indeed exists a myriad and complex network of MAPs in higher eukaryotes that may play roles similar to that of She1. For instance, the mammalian tau-related MAP4 protein, which binds in close proximity to G436 (Shigematsu et al., 2018), has been implicated in the control of dynein-mediated spindle orientation during mitosis in mammalian cells (Samora et al., 2011). MAP4 was also shown to physically interact with dynein–dynactin in vivo and to inhibit dynein-mediated microtubule gliding in vitro (Samora et al., 2011). MAP4 has also been shown to shorten dynein-dependent runs of melanosomes in *Xenopus* melanophores (Semenova et al., 2014). Another potential functional homologue of She1 is MAP9 (also known as ASter-Associated Protein, or ASAP), depletion of which disrupts spindle organization (Saffin et al., 2005; Venoux et al., 2008) and which was recently shown to inhibit processive motility of purified dynein–dynactin complexes by specifically precluding microtubule binding by dynactin (Monroy et al., 2020). Thus, it will be important to determine how TUBA1A^{G436R} affects binding of these important neuronal MAPs.

MATERIALS AND METHODS

[Request a protocol](#) through *Bio-protocol*.

Plasmids, yeast strain growth, and genetic manipulation

Strains used in this study were isogenic to either BY4742 (for Figures 1, 2, A and B, 4, and 5; *MAT α* ; *ura3 Δ 0 leu2 Δ 0 his3 Δ 1 lys2 Δ 0*; provided by euroscarf, <http://www.euroscarf.de>) or YEF473 (for Figures 3 and 6–8; *ura3-52 lys2-801 leu2- Δ 1 his3- Δ 200 trp1- Δ 63*). The *TUB1* integrating plasmid, pCR2-TUB1, consists of the region of the *TUB1* locus from the intron (situated close to the 5' end of the gene) to 385 base pairs after the stop codon cloned into the pCR2 vector (Invitrogen). The *HIS3* gene expression cassette was ligated into the *BsrGI* site within the 3' untranslated region of the *TUB1* sequence within pCR2 (pCR2-TUB1). The G437R mutation was subsequently

introduced into pCR2-TUB1 by PCR, generating pCR2-*tub1*^{G437R}. For integration into the native *TUB1* locus, pCR2-TUB1 (either wild type or mutant) was digested with *SphI*, transformed into yeast using the lithium acetate method, and transformants were selected on media lacking histidine. All transformants were confirmed by PCR and sequencing.

RFP-TUB1 and *RFP-tub1*^{G437R} (under control of the *TUB1* promoter; employed in Figures 1C and 5CE), are derived from pAF125 (Straight et al., 1997), as previously described (Caudron et al. 2008). In addition to this construct, we also generated pHIS3p:*mRuby2-tub1*^{G437R}+3'UTR::*LEU2* to visualize microtubules in mutant cells (employed in Figure 3, C and D). To this end, we engineered the G437R point mutation into pHIS3p:*mRuby2-TUB1*+3'UTR::*LEU2* (Markus et al., 2015) using traditional molecular biological methods. For comparison of relative α -tubulin incorporation into mitotic spindles, we used yeast strains with similarly integrated mRuby2- α -tubulins (pHIS3p:*mRuby2-TUB1*+3'UTR::*LEU2* or pHIS3p:*mRuby2-tub1*^{G437R}+3'UTR::*LEU2*). To assess the relative incorporation of Tub3 into the mitotic spindle, we replaced the *TUB1*+3'UTR cassette in pHIS3p:*mRuby2-TUB1*+3'UTR::*TRP1* (Markus et al., 2015) with the *TUB3* genomic sequence, including 150 base pairs of the 3'UTR (note that both *mRuby2-TUB1* and *mRuby2-TUB3* possess the same glycine–serine linker between the mRuby2 and the tubulin). This plasmid, pHIS3p:*mRuby2-TUB3*+3'UTR::*TRP1*, was digested with *BbvCI* and transformed into yeast using the lithium acetate method, and transformants were selected on media lacking tryptophan. Before imaging cells with these chromosomally integrated FP-Tub1 plasmids, cells were grown in synthetic defined complete media (i.e., histidine was indeed included in the growth media, omission of which would potentially lead to increased levels of expression from the *HIS3* promoter [Kim and Clark, 2002]). Vectors to generate GFP-Bim1 (pB1225) and Bik1-GFP (pB681) were kindly provided by D. Pellman (Dana-Farber Cancer Institute, Boston, MA; Tirnauer et al., 1999; Lin et al., 2001).

For the two-hybrid experiments, the *TUB1* or *tub1*^{G437R} open reading frames from the respective pCR2 vectors (see above) were cloned into the pLexA vector (Addgene) to produce LexA_{DBD}-Tub1 (or LexA_{DBD}-Tub1^{G437R}) fusion proteins with a-tubulin and the DNA-binding domain of LexA (LexA_{DBD}). Bim1, Kip3, and She1 were amplified from genomic DNA and cloned into the pGADT7 vector (Invitrogen) to produce fusion proteins with the GAL4-activating domain (GAL4_{AD}).

The 6His-tagged-She1^{Cter} expression plasmid was constructed in the pET28 vector (Novagen). The She1 C-terminal part coding for amino acids 194–338 was ligated between the *NdeI* and *XhoI* sites of the vector downstream of the 6His and thrombin site.

To generate a GFP11_{x7}-She1-expressing yeast strain (She1 fused to seven copies of strand 11 of GFP) (Kamiyama et al., 2016), the GFP11_{x7} cassette was PCR amplified from pACUH:GFP11_{x7}-mCherry- β -tubulin (Addgene, plasmid # 70218) and integrated at the 5' end of the *SHE1* open reading frame using the sequential *URA3* selection/5-FOA (5-fluoroorotic acid) counterselection method. To separately express strands 1–10 of the GFP barrel (GFP₁₋₁₀, which is required to reconstitute fluorescence), we generated a plasmid with an expression cassette encoding GFP₁₋₁₀ under the control of the strong *TEF1* promoter (*TEF1*p), as well as the *TRP1* selectable marker (pRS304:TEF1p:GFP₁₋₁₀). We PCR amplified the *TEF1*p:GFP1-10::*TRP1* cassette and integrated it into the *lys2-801* locus using homologous recombination into the GFP11_{x7}-She1-expressing yeast strain.

To express a second copy of *TUB3* from the genome, the sequence corresponding to TUB3 and 153 nucleotides of the 3' UTR

was amplified from pHis3p:mRuby2-TUB3+3'UTR::TRP1 (described above) and assembled into pRS306 digested with *KpnI* and *NotI* along with a second PCR product corresponding to the TEF1 promoter using isothermal assembly (Gibson *et al.*, 2009). This plasmid, pRS306: TEF1p:TUB3+3'UTR, was digested with *Apal* (cuts within the *URA3* gene, leading to integration at the *ura3-52* locus) and transformed into yeast using the lithium acetate method, and transformants were selected on media lacking uracil.

To assess viability on solid media (Figure 1D), serial dilutions of fresh overnight cultures of wild-type or *tub1*^{G437R} cells (three different haploid clones for each strain) were spotted onto solid yeast extract peptone adenine dextrose (YPAD) media with or without benomyl, as indicated. Plates were incubated for 2 d at 30°C.

Image acquisition and analysis

Cell imaging was performed on either a Zeiss Axiovert microscope equipped with a Cool Snap ES CCD camera (Roper Scientific; for Figures 1, 2, and 4 and Supplemental Figures S3 and S4) or Nikon Ti-E microscope equipped with a 1.49 NA 100× total internal reflection fluorescence (TIRF) objective, a Ti-S-E motorized stage, piezo Z-control (Physik Instrumente), an iXon DU888 cooled EM-CCD camera (Andor), a stage-top incubation system (Okolab), and a spinning-disk confocal scanner unit (CSUX1; Yokogawa) with an emission filter wheel (ET525/50M for GFP and ET632/60M for mRuby2; Chroma; Figures 3, 7, and 8). For Figures 1, 2, and 4, 11 Z-planes with 0.3 μm spacing were captured using 2 × 2 binning (the exposure time varied between experiments). For Figures 3, 7, and 8, 15 or 17 Z-planes with 0.2 μm spacing were captured. TIRF microscopy (to image *in vitro* reconstituted microtubules from purified protein or cell extracts; Figures 6 and 7 and Supplemental Figure S5) was performed with a 1.49 NA 100× TIRF objective on a Nikon Ti-E inverted microscope equipped with a Ti-S-E motorized stage, piezo Z-control (Physik Instrumente), and an iXon X3 DU897 cooled EM-CCD camera (Andor). Lasers (488, 561, and 640 nm) (Coherent) were used along with a multipass quad filter cube set (C-TIRF for 405/488/561/638 nm; Chroma) and emission filters mounted in a filter wheel (525/50, 600/50, and 700/75 nm; Chroma).

For *in vivo* microtubule dynamics measurements, maximum-intensity projection images of Bik1-GFP-expressing cells were used. Ten-minute movies were acquired with an acquisition frequency of six frames per minute. Microtubule lengths at each time point were measured manually from maximum-intensity projections, and microtubule dynamic parameters were calculated as described (Kosco *et al.*, 2001), using an in-house Visual Basic macro in Excel (Caudron *et al.*, 2008). We measured background-corrected She1, Tub1, or Tub3 spindle-localized fluorescence from maximum-intensity projections using ImageJ (National Institutes of Health). Tub1-corrected She1 intensities were calculated by normalizing the fluorescence intensity values of each (She1, Tub1, and Tub3) to 1 (by dividing the raw mean background-corrected values for that measured in wild-type or *tub1*^{G437R} cells by the wild-type value) and then dividing the resulting normalized She1 values by the normalized Tub1 value for wild type and *tub1*^{G437R}, respectively. To additionally correct for Tub3 intensities, these Tub1-corrected values were then divided by the normalized Tub3 values (as calculated above; in which wild type = 1 and *tub1*^{G437R} = 1.91).

To assess spindle dynamics parameters, we determined spindle position in cells over time by clicking the center of a preanaphase spindle in each frame and calculating the displacement between frames using an in-house-developed ImageJ macro. Microtubule lengths during sliding events were manually measured at each time point from maximum-intensity projections. Catastrophe events were

defined as “following a sliding event” (Figure 4E) if they occurred during the 1 min period following the cessation of a sliding event. The spindle position with respect to the cell boundaries, as shown in Figure 4G, was determined for spindles with a pole-to-pole length of 0.8–1.2 μm from the first frames of movies of G2/M cells. The quantification was done blind to the genotype. At least 52 preanaphase spindles from three independent clones were measured for each strain, as described (DeZwaan *et al.*, 1997). Spindle positioning was similarly determined from single time-point images acquired of hydroxyurea-arrested cells for data shown in Supplemental Figure S6C.

Assessment of cell cycle progression (see Figure 8) was performed by imaging cells in the CellAsic ONIX system using microfluidic cassettes designed for haploid yeast cells (Y04C; Millipore-Sigma) on a spinning-disk confocal scanner unit (CSUX1; Yokogawa) with an emission filter wheel (ET525/50M for yellow fluorescent protein [YFP]) using a 100× oil-immersion objective. In brief, after an overnight growth in synthetic defined (SD) complete media (supplemented with 2% glucose) at 30°C, cells were diluted twofold and grown for 5 h before a 50-fold dilution into the cell inlet well of the microfluidic cassette, which was primed with SD complete before the addition of cells (per the manufacturer's instructions). Pressure was maintained at 7.0 psi throughout the imaging period to ensure a constant replenishment of media into the cassette, which was set to 30°C. Wild-type and mutant cells were imaged simultaneously by introducing respective cells into adjacent imaging chambers of the microfluidics cassette. Z-stacks (seven steps with 0.5 μm spacing) from five XY coordinates for each strain were acquired for 10–12 h at 90 s intervals.

Cell lysis and immunoblotting

Yeast cultures were grown overnight at 30°C in 3 ml of YPAD. The next morning, 1 ml of overnight culture was added to 2 ml fresh YPAD and grown at 30°C for 1.5 h before harvesting. Equal numbers of cells were pelleted and resuspended in 0.2 ml of 0.1 M NaOH and incubated for 5 min at room temperature as described (Kushnirov, 2000). After centrifugation, the resulting cell pellet was resuspended in sample buffer and heated to 100°C for 3 min. After clarification (1 min at 15,000 rpm), lysates were separated on a 10% SDS-polyacrylamide gel. Before electroblotting to polyvinylidene fluoride (PVDF) (for 32 min at 100 V in 25 mM Tris, 192 mM glycine supplemented with 0.05% SDS and 10% methanol), acrylamide gels were imaged for total protein using Bio-Rad Stain-Free technology (on a Bio-Rad Chemidoc gel documentation system). The fluorescence intensity of these bands was used to correct for differences in potential loading differences in each lane. PVDF membranes were probed with 1:2000 rat (YL1/2; in-house production) or 1:100 mouse (4A1; registry AB_2732839 from DSHB) anti-α-tubulin antibodies, and either horseradish peroxidase-conjugated goat anti-rat (Jackson ImmunoResearch Laboratories 712-605-153) or IRDye 800CW goat anti-mouse antibodies (Li-Cor 925-32210) used at 1:2000 and 1:15,000, respectively. Chemiluminescence signals were acquired on a Bio-Rad Chemidoc MP, and fluorescence signals were acquired on an Odyssey CLx imaging system. Immunoblots were imaged without saturating the camera's pixels. Band intensity and background correction was done using ImageJ for both chemiluminescence and fluorescence. Bio-Rad Stain-Free gel signal was used to correct for differences in lysate loading between lanes.

Electron tomography of yeast cells

Cells were processed for electron microscopy using methods described previously (Winey *et al.*, 1995; Giddings *et al.*, 2001). Briefly,

aliquots of log phase cultures were collected by vacuum filtration and frozen using a Wohlwend Compact 02 high-pressure freezer (Technotrade International, Manchester, NH). The frozen cells were freeze-substituted in 1% osmium tetroxide and 0.1% uranyl acetate in acetone and then embedded in Epon/Araldite resin (Electron Microscopy Sciences, Fort Washington, PA). Serial semithick (250 nm) sections were cut using a Leica Ultracut-E microtome and collected onto Formvar-coated copper slot grids. The sections were post-stained with 2% aqueous uranyl acetate followed by Reynolds lead citrate. Fifteen-nanometer colloidal gold particles (Ted Pella) were affixed to both surfaces of the section to serve as fiducial markers for tilt-series alignment.

Tomography was performed as described (O'Toole *et al.*, 2002). Dual-axis tilt series were collected using a Tecnai F30 microscope (ThermoFisher Scientific, Waltham, MA) using the SerialEM program for data acquisition (Mastronarde, 2005). Tilt-series data were acquired from serial sections at a pixel size of 1.2 nm using a Gatan One View camera (Gatan, Pleasanton, CA). Tomographic volumes were computed using the IMOD software package (Kremer *et al.*, 1996; Mastronarde, 1997). For each spindle, volumes from three to four serial sections were joined, and the spindle microtubules were modeled using the 3dmod program of the IMOD software package. Microtubule number, lengths, and SPB diameters were computed from the model contour data. The mtpairing program of the IMOD software package was used to compute and identify the core bundle mts in each spindle (Winey *et al.*, 1995). In total, two spindles from wild-type cells, two spindles from *tub1^{G437R}* cells, and five spindles from "Tub3-only" (*TEF1p :TUB3 tub1Δ*) cells were reconstructed and analyzed.

Production of recombinant protein

The 6His-She1^{Cter} plasmid was transformed into Rosetta pLysS bacteria. For protein production, bacterial cultures grown in M9 medium were induced by the addition of 1 mM isopropyl β-D-1-thiogalactopyranoside (IPTG) overnight at 18°C. The clarified lysate was separated on a cation exchange column (SP GE healthcare), and bound protein was eluted in cation elution buffer (500 mM NaCl, 40 mM Tris, pH 9.2) and then applied to a NiNTA column (Qiagen) after the addition of 20 mM imidazole. After elution in NiNTA elution buffer (300 mM NaCl, 20 mM Tris, pH 7.5, 250 mM imidazole), the protein was simultaneously concentrated and buffer-exchanged (with a Vivaspin Turbo 4; Sartorius) into PM buffer (80 mM PIPES, pH 6.8, 1 mM MgCl₂, 0.2% NP40).

Purification of yeast tubulin was performed essentially as described (Johnson *et al.*, 2011) with minor modifications. Yeast cells (JEL1) cotransformed with p426Gal1:Tub1 (or p426Gal1:Tub1^{G437R}) and p424:Tub2-6His were grown in 5 ml of selective SD complete media (lacking uracil and tryptophan) supplemented with 2% glucose for 3 d at 30°C before being transferred to 50 ml of identical media for 1 d. The 50 ml cultures were then transferred to 1 l of nonselective YPGL (2% peptone, 1% yeast extract, 3% glycerol, and 2% lactate; note that we grew 16 l of cells for a typical prep). When the cell density reached an OD₆₀₀ between 5 and 9 (approximately 20–24 h later), 20 g of galactose powder was added per liter of YPGL, and after 5 h, cells were harvested, washed with water, and stored at –80°C. Cells (approximately 75 g) were thawed and resuspended in 70 ml of lysis buffer (50 mM HEPES, pH 7.4, 500 mM NaCl, 10 mM MgSO₄, 30 mM imidazole) supplemented with 50 μM GTP and cOmplete protease inhibitor cocktail (Roche) and lysed by five to six passes through a microfluidizer (LM10; Microfluidics) at 23,000 psi, with 5 min on ice between each pass. After clarification (at 13,000 rpm for 30 min at 4°C), the supernatant was

applied to a 5 ml HisTrap Ni-NTA column (GE) preequilibrated with 10 column volumes (CVs) of lysis buffer supplemented with GTP using an AKTA FPLC (GE). After washing the column with 10 CVs of lysis buffer supplemented with 50 μM GTP and 10 CVs of nickel wash buffer (25 mM PIPES, pH 6.9, 1 mM MgSO₄, 30 mM imidazole) supplemented with 50 μM GTP, bound protein was eluted with six CVs of elution buffer (25 mM PIPES, pH 6.9, 1 mM MgSO₄, 300 mM imidazole) supplemented with 50 μM GTP. Peak fractions (determined by absorbance at 260 nm) were pooled and treated with nuclease (Pierce Universal Nuclease; catalogue #88702; 10 μl per 20 ml of eluate) for 15 min at room temperature and then diluted with MonoQ buffer A (25 mM PIPES, pH 6.9, 2 mM MgSO₄, 1 mM ethylene glycol-bis(β-aminoethyl ether)-N,N,N',N'-tetraacetic acid (EGTA) supplemented with 50 μM GTP such that the final imidazole concentration was 100 mM. The protein was then loaded onto a MonoQ 10/100GL anion exchange column preequilibrated with five CVs of 90% MonoQ buffer A (see above) and 10% MonoQ buffer B (25 mM PIPES, pH 6.9, 2 mM MgSO₄, 1 mM EGTA, 1 M NaCl) supplemented with 50 μM GTP, after which bound protein was eluted using with a 10–70% MonoQ buffer B gradient over 50 CVs. Peak tubulin fractions (determined by absorbance at 260 nm and SDS-PAGE) were pooled and concentrated (Amicon Ultra-4 30K; catalogue #UFC803024) to approximately 2.8–3.0 μM (concentration and aggregation were closely monitored using absorbance at 260 and 280 nm) and then dialyzed against tubulin storage buffer (10 mM PIPES, pH 6.9, 1 mM MgSO₄, 1 mM EGTA) supplemented with 50 μM GTP (Thermo Slide-A-Lyzer; catalogue #66810). The resulting protein was aliquoted (50 μl), snap frozen in liquid nitrogen, and stored at –80°C.

We purified She1-HaloTag from protease-deficient budding yeast transformed with pBJ1153:ARSH/CEN:GAL1p:8xHis-ZZ-2xTEV-She1-HaloTag. Cells were grown at 30°C in 3 ml YPA media supplemented with 2% glucose and 100 μg/ml G418 (to select for the plasmid) for 16 h. The 3 ml culture was transferred to 40 ml YPA media supplemented with 2% glucose and 100 μg/ml G418 and grown at 30°C for 8 h before being transferred to 1 l YPA media supplemented with 2% raffinose and 100 μg/ml G418. After 16 h at 30°C, the cells were transferred to sterile centrifuge bottles and centrifuged to remove media. Cells were then resuspended in 1 l YPA media supplemented with 2% galactose and 100 μg/ml G418 and grown at 30°C for 5–6 h before harvesting, washing with water, and storing at –80°C. Cells were thawed in a 0.5 volume of cold 2x lysis buffer (1x buffer: 30 mM HEPES, pH 7.2, 50 mM potassium acetate, 2 mM magnesium acetate, 0.2 mM EGTA, 10% glycerol, 1 mM dithiothreitol (DTT), and protease inhibitor tablets [Pierce]) and then lysed by five passes through a microfluidizer (LM10; Microfluidics) at 23,000 psi, with 5 min on ice between each pass. The lysate was clarified at 22,000 × g for 20 min, adjusted to 0.005% Triton X-100, and then incubated with immunoglobulin G Sepharose agarose beads for 1 h at 4°C. The resin was then washed three times with wash buffer (30 mM HEPES, pH 7.2, 50 mM potassium acetate, 2 mM magnesium acetate, 0.2 mM EGTA, 300 mM KCl, 0.005% Triton X-100, 10% glycerol, 1 mM DTT, protease inhibitor tablets) and twice in TEV digest buffer (10 mM Tris, pH 8.0, 150 mM KCl, 0.005% Triton X-100, 10% glycerol, 1 mM DTT). To fluorescently label She1-HaloTag, the bead-bound protein was incubated with 6.7 μM HaloTag-TMR ligand (Promega) for 15 min at room temperature. The resin was then washed three more times in TEV digest buffer to remove unbound ligand and then incubated in TEV buffer supplemented with TEV protease for 1 h at 16°C. The resulting eluate was collected using a centrifugal filter unit (0.1 μm; Millipore), aliquoted, drop frozen in liquid nitrogen, and stored at –80°C.

Liquid chromatography-coupled tandem mass spectrometry

Approximately 10 µg of purified wild-type or G437R mutant tubulin (purified as described above from budding yeast) was denatured, reduced, and alkylated in freshly prepared 5% (wt/vol) SDS, 10 mM tris(2-carboxyethyl-phosphine) (TCEP), and 40 mM 2-chloroacetamide (CIAA) by boiling for 10 min at 95°C. Sample preparation for mass spectrometry analyses was performed using the SP3 method (Hughes *et al.*, 2014). Briefly, Sera-Mag SpeedBead carboxylate-modified magnetic beads (200 µg; Cytiva) were added to denatured and reduced tubulin samples and then mixed thoroughly. Acetonitrile was added to 80% (vol/vol) and mixed for 10 min to precipitate protein. Tubes were placed on a magnet, and the supernatant was removed. Beads were then washed two times with 80% (vol/vol) ethanol and two times with 100% acetonitrile, by incubating in a sonicating water bath for 2 min per wash. Protease digestion was performed with 0.5 µg of a LycC/Trypsin mix (Promega) in 25 µl 50 mM Tris, pH 8.5, with mixing overnight at 37°C. To remove the buffer from the tryptic peptides, acetonitrile was added to 95% (vol/vol) to precipitate peptides. One wash with 100% acetonitrile was performed, and tryptic peptides were eluted twice with 1% (vol/vol) trifluoroacetic acid (TFA), 3% (vol/vol) acetonitrile in LC/MS grade water. Elutions were dried using a speed-vac rotatory evaporator and resuspended in 0.1% TFA, 3% acetonitrile in water. Peptides were directly injected onto a Waters M-class column (1.7 µm, 120 Å, rpC18, 75 µm × 250 mm) and gradient eluted from 2% to 40% acetonitrile over 40 min at 0.3 µl/min using a Thermo Ultimate 3000 UPLC (Thermo Scientific). Peptide ions were detected with a Thermo Q-Exactive HF-X mass spectrometer (Thermo Scientific) scanning MS1 spectra at 120,000 resolution from 380 to 1580 m/z with a 45 ms fill time and 3E6 AGC target. The top 12 most intense peaks were isolated with 1.4 m/z window with a 100 ms fill time and 1E6 AGC target and 27% HCD collision energy for MS2 spectra collected at 15,000 resolution. Dynamic exclusion was enabled for 5 s. MS data raw files were searched against the Uniprot *Saccharomyces cerevisiae* database UP000002311 (downloaded on 4/16/2021) using Maxquant 1.6.14.0 with cysteine carbamidomethylation as a fixed modification, while methionine oxidation and protein N-terminal were set as variable modifications. The mass tolerances for the database search were 4.5 ppm for the MS1 precursors and 20 ppm for the MS2 fragment ions; the minimum peptide length was seven residues. Peptide and protein level false discovery rate was 0.01.

Pull-down experiments

For She1^{C-term}-tubulin pull-down experiments, 2.5 µg of purified tubulin (from cow brain) was incubated with or without 2.5 µg of 6His-She1^{C-term} in 500 µl of PM buffer. After 30 min at room temperature, NiNTA beads (10 µl) were added (Thermo Fisher). After a 10 min incubation, the beads were washed three times with PM buffer and then boiled for 5 min in 60 µl of sample buffer before SDS-PAGE analysis. For peptide competition experiments, 50 µg of each peptide (dissolved in PM buffer; wild type: EEGEFTEAREDLAALRDYIEVGADSYAE EEEEF; G437R: EEGEFTEAREDLAALRDYIEVRADSYAE EEEEF) was added to the mixture of She1^{C-term} (0.25 µg; resulting in an approximately 900-M excess of peptide with respect to She1^{C-term}) and tubulin (1.25 µg) and allowed to bind for 30 min at room temperature. Then, NiNTA beads (10 µl) were added (Thermo Fisher), incubated for 10 min, washed three times with PM buffer, and then boiled for 5 min in 60 µl of sample buffer before SDS-PAGE and immunoblot analysis. For immunoblotting, the gel was transferred to a PVDF membrane (BioRad TransBlot Turbo), blocked with phosphate-buffered saline supplemented with 5% milk

for 30 min, and then probed with anti- α -tubulin (YL1/2 1:10,000) followed by Cy5 anti-rat secondary antibody (Jackson ImmunoResearch; 1:2000). To quantify the tubulin signals, the local background was subtracted and signals were normalized such that tubulin-bound 6His-She1^{C-term} without peptide was equal to 100. The average of two replicates is presented in the graph (Figure 6C).

Microtubule reconstitutions using cell lysates

Microtubules were polymerized from preassembled coverslip-immobilized microtubule seeds and concentrated cell extracts as previously described (Bergman *et al.*, 2018), but with minor modifications. Overnight cultures of cells (3 ml in YPAD media) with respective α -tubulin content (e.g., wild type, *tub1*^{G437R}) were diluted into 200 ml of YPAD and grown for 16 h before being transferred to 800 ml of YPAD. Cultures were grown for 30 min before treatment with 100 mM hydroxyurea (to synchronize the cells in a cell cycle amenable to microtubule polymerization activity). After a 2.5 h incubation in hydroxyurea, cells were pelleted, washed once with water, then drop frozen in liquid nitrogen after removing residual liquid, and stored at -80°C until lysis. Frozen cells (approximately 4 g) were lysed in a prechilled midsize cryogenic impact mill (SPEX model 6875). Milling consisted of a 3 min prechill followed by 10 cycles comprising 3 min of grinding at 30 impacts per second (15 cps) and 1 min of rest. The sample vial remained submerged in liquid nitrogen throughout the lysis process. Frozen, powdered lysate was recovered and stored at -80°C until use.

Microtubule seeds were prepared by incubating a mixture of unlabeled and rhodamine-labeled porcine tubulin (Cytoskeleton; resuspended at 5 and 1 mg/ml, respectively, in PEM80: 80 mM PIPES, pH 6.9, 1 mM EGTA, 1 mM MgCl₂) with 1 mM GMPCPP (Jena Biosciences) at 37°C for 10 min. Microtubule seeds were adhered to imaging chambers assembled from a glass slide, double-stick tape, and a plasma-cleaned and silanized glass coverslip using an anti-rhodamine antibody (1:10 dilution incubated for 10 min; Thermo Fisher; catalogue #200-301-246). Seeds were diluted 1:100 in MT seed mix (PEM80, 5 mg/ml casein, oxygen scavenging mix, 5 mM β -mercaptoethanol, 0.4% methylcellulose). Following antibody incubation, the chamber was washed with wash buffer (PEM80 supplemented with oxygen scavenging mix and 5 mM β -mercaptoethanol) before adding diluted seed mix. Seeds were incubated for approximately 5 min before an additional wash with wash buffer, after which the chamber was ready for addition of lysate.

To prepare lysate, 0.5 µl of Protease Inhibitor Cocktail IV (Calbiochem) was added to approximately 0.5 g of frozen powdered lysate that was transferred to a liquid nitrogen prechilled polycarbonate ultracentrifuge tube. After thawing on ice for 10 min, the lysate was then clarified by centrifuging at 346,000 × g for 25 min at 4°C (in a TLA-100 rotor). To polymerize microtubules, lysate supplemented with 0.5 mM GTP (from 20 mM GTP stock) was introduced into the chamber and incubated for 15 min in a stage-top incubator prewarmed to 28°C. Microtubule growth from coverslip-adhered seeds was monitored by interference fluorescence microscopy (IRM; see Supplemental Figure S5D) as described previously (Mahamdeh *et al.*, 2018). To assess She1-microtubule binding, 1 µl of full-length She1-HaloTag⁶⁶⁰ diluted in 7 µl of clarified lysate (supplemented with 0.5 mM GTP) was then introduced into the imaging chamber with the polymerized microtubules (note that each chamber accommodates approximately 7–8 µl in volume; thus, ~1 chamber volume of She1-supplemented lysate was introduced into each chamber). Lysate was used instead of buffer to ensure that sufficient tubulin concentrations were present to prevent coverslip-immobilized

microtubules from depolymerizing. Images of She1-HaloTag⁶⁶⁰, microtubules (acquired using IRM; see Supplemental Figure S5D, for example) and rhodamine seeds were acquired using TIRF microscopy immediately following addition into a chamber (all images were acquired within 3 min of adding She1). Using ImageJ, lines drawn along the length of single, nonbundled microtubules (identified in the IRM channel) were used to determine the mean fluorescence intensity per pixel. Overlapping and/or intersecting microtubules were omitted from our measurements, as were microtubule seed regions, to which we noted She1 binds to a significantly lower extent (e.g., see arrowheads in Figure 6D). Approximately four to six different fields were acquired to control for potential variation between fields of view. To control for potential regional She1 concentration differences within each chamber, images were generally acquired within the middle of each, a significant distance from the sample loading area. Note that replicates were performed on different days.

Structural analyses and mutation modeling

Molecular graphics and analyses were performed with the UCSF Chimera package. The rotamers function was used to model an arginine substitution into position 436 of the α -tubulin structure (PDB 3J6G). The top four rotamers were selected for visualization (see Supplemental Figure S2).

ACKNOWLEDGMENTS

We thank Jeff Moore for kindly providing a tub3 Δ yeast strain, Luke Rice for invaluable assistance with the yeast tubulin purification, and members of the Georjana Barnes lab for advice regarding the lysate-based microtubule reconstitution assay. Electron microscopy and mass spectrometry were performed at the University of Colorado, Boulder, at the EM Services Core Facility in the MCDB Department and the Central Analytical Mass Spectrometry Lab, respectively, with the technical assistance of the staff. This work was funded by INCA (TetraTips PLBIO10-030 to A.A. and C.B.) and the National Institutes of Health/National Institute of General Medical Sciences (NIGMS) (R01GM118492 and R35GM139483 to S.M.M.). Chimera is developed by the Resource for Biocomputing, Visualization, and Informatics at the University of California, San Francisco (supported by NIGMS P41-GM103311).

REFERENCES

Adames NR, Cooper JA (2000). Microtubule interactions with the cell cortex causing nuclear movements in *Saccharomyces cerevisiae*. *J Cell Biol* 149, 863–874.

Aiken J, Sept D, Costanzo M, Boone C, Cooper JA, Moore JK (2014). Genome-wide analysis reveals novel and discrete functions for tubulin carboxy-terminal tails. *Curr Biol* 24, 1295–1303.

Alushin GM, Lander GC, Kellogg EH, Zhang R, Baker D, Nogales E (2014). High-resolution microtubule structures reveal the structural transitions in α -tubulin upon GTP hydrolysis. *Cell* 157, 1117–1129.

Badin-Larcon AC, Boscheron C, Soleilhac JM, Piel M, Mann C, Denarier E, Fourest-Lieuvain A, Lafanechere L, Bornens M, Job D (2004). Suppression of nuclear oscillations in *Saccharomyces cerevisiae* expressing Glu tubulin. *Proc Natl Acad Sci USA* 101, 5577–5582.

Bahi-Buisson N, Cavallin M (1993). Tubulinopathies overview. In *GeneReviews*, MP Adam, HH Ardinger, RA Pagon, SE Wallace, LJM Bean, K Stephens, and A Amemiya, ed., Seattle: University of Washington.

Bahi-Buisson N, Poirier K, Boddart N, Saillour Y, Castelnaud L, Philip N, Buyse G, Villard L, Joriot S, Marret S, et al. (2008). Refinement of cortical dysgenesis spectrum associated with TUBA1A mutations. *J Med Genet* 45, 647–653.

Bahi-Buisson N, Poirier K, Fourniol F, Saillour Y, Valence S, Lebrun N, Hully M, Bianco CF, Boddart N, Elie C, et al. (2014). The wide spectrum of tubulinopathies: what are the key features for the diagnosis? *Brain* 137, 1676–1700.

Bergman ZJ, Wong J, Drubin DG, Barnes G (2018). Microtubule dynamics regulation reconstituted in budding yeast lysates. *J Cell Sci* 132, jcs219386.

Bieling P, Kandels-Lewis S, Telley IA, van Dijk J, Janke C, Surrey T (2008). CLIP-170 tracks growing microtubule ends by dynamically recognizing composite EB1/tubulin-binding sites. *J Cell Biol* 183, 1223–1233.

Bode CJ, Gupta ML, Suprenant KA, Himes RH (2003). The two α -tubulin isotypes in budding yeast have opposing effects on microtubule dynamics in vitro. *EMBO Rep* 4, 94–99.

Bowman AB, Kamal A, Ritchings BW, Philp AV, McGrail M, Gindhart JG, Goldstein LS (2000). Kinesin-dependent axonal transport is mediated by the sundry driver (SYD) protein. *Cell* 103, 583–594.

Breuss M, Heng JI, Poirier K, Tian G, Jaglin XH, Qu Z, Braun A, Gstrein T, Ngo L, Haas M, et al. (2012). Mutations in the beta-tubulin gene TUBB5 cause microcephaly with structural brain abnormalities. *Cell Rep* 2, 1554–1562.

Brouhard GJ, Stear JH, Noetzel TL, Al-Bassam J, Kinoshita K, Harrison SC, Howard J, Hyman AA (2008). XMAP215 is a processive microtubule polymerase. *Cell* 132, 79–88.

Burke D, Gasdaska P, Hartwell L (1989). Dominant effects of tubulin overexpression in *Saccharomyces cerevisiae*. *Mol Cell Biol* 9, 1049–1059.

Carminati JL, Stearns T (1997). Microtubules orient the mitotic spindle in yeast through dynein-dependent interactions with the cell cortex. *J Cell Biol* 138, 629–641.

Caudron F, Andrieux A, Job D, Boscheron C (2008). A new role for kinesin-directed transport of Bik1p (CLIP-170) in *Saccharomyces cerevisiae*. *J Cell Sci* 121, 1506–1513.

Ciferri C, Pasqualato S, Screpanti E, Varetto G, Santaguida S, Dos Reis G, Maiolica A, Polka J, De Luca JG, De Wulf P, et al. (2008). Implications for kinetochore-microtubule attachment from the structure of an engineered Ndc80 complex. *Cell* 133, 427–439.

Cushion TD, Paciorek AR, Pilz DT, Mullins JG, Seltzer LE, Marion RW, Tuttle E, Ghoneim D, Christian SL, Chung SK, et al. (2014). De novo mutations in the beta-tubulin gene TUBB2A cause simplified gyral patterning and infantile-onset epilepsy. *Am J Hum Genet* 94, 634–641.

Del Bene F, Wehman AM, Link BA, Baier H (2008). Regulation of neurogenesis by interkinetic nuclear migration through an apical-basal notch gradient. *Cell* 134, 1055–1065.

Denarier E, Brousse C, Sissoko A, Andrieux A, Boscheron C (2019). A neurodevelopmental TUBB2B beta-tubulin mutation impairs Bim1 (yeast EB1)-dependent spindle positioning. *Biol Open* 8, bio038620.

DeZwaan TM, Ellingson E, Pellman D, Roof DM (1997). Kinesin-related KIP3 of *Saccharomyces cerevisiae* is required for a distinct step in nuclear migration. *J Cell Biol* 138, 1023–1040.

Di Donato N, Timms AE, Aldinger KA, Mirzaa GM, Bennett JT, Collins S, Olds C, Mei D, Chiari S, Carvill G, et al. (2018). Analysis of 17 genes detects mutations in 81% of 811 patients with lissencephaly. *Genet Med* 20, 1354–1364.

Eckert T, Le DT, Link S, Friedmann L, Woelke G (2012). Spastin's microtubule-binding properties and comparison to katanin. *PLoS One* 7, e50161.

Ecklund KH, Morisaki T, Lammers LG, Marzo MG, Stasevich TJ, Markus SM (2017). She1 affects dynein through direct interactions with the microtubule and the dynein microtubule-binding domain. *Nat Commun* 8, 2151.

Estrem C, Fees CP, Moore JK (2017). Dynein is regulated by the stability of its microtubule track. *J Cell Biol* 216, 2047–2058.

Fees CP, Aiken J, O'Toole ET, Giddings TH Jr, Moore JK (2016). The negatively charged carboxy-terminal tail of beta-tubulin promotes proper chromosome segregation. *Mol Biol Cell* 27, 1786–1796.

Findeisen P, Muhlhausen S, Dempewolf S, Hertzog J, Zietlow A, Carlomagno T, Kollmar M (2014). Six subgroups and extensive recent duplications characterize the evolution of the eukaryotic tubulin protein family. *Genome Biol Evol* 6, 2274–2288.

Fourel G, Boscheron C (2020). Tubulin mutations in neurodevelopmental disorders as a tool to decipher microtubule function. *FEBS Lett* 594, 3409–3438.

Fu MM, Holzbaur EL (2013). JIP1 regulates the directionality of APP axonal transport by coordinating kinesin and dynein motors. *J Cell Biol* 202, 495–508.

Fukuda Y, Luchniak A, Murphy ER, Gupta ML Jr (2014). Spatial control of microtubule length and lifetime by opposing stabilizing and destabilizing functions of kinesin-8. *Curr Biol* 24, 1826–1835.

Gardner MK, Haase J, Myhre K, Molk JN, Anderson M, Joglekar AP, O'Toole ET, Winey M, Salmon ED, Odde DJ, Bloom K (2008). The microtubule-based motor Kar3 and plus end-binding protein Bim1 provide structural support for the anaphase spindle. *J Cell Biol* 180, 91–100.

- Gartz Hanson M, Aiken J, Sietsema DV, Sept D, Bates EA, Niswander L, Moore JK (2016). Novel alpha-tubulin mutation disrupts neural development and tubulin proteostasis. *Dev Biol* 409, 406–419.
- Gibson DG, Young L, Chuang RY, Venter JC, Hutchison CA 3rd, Smith HO (2009). Enzymatic assembly of DNA molecules up to several hundred kilobases. *Nat Methods* 6, 343–345.
- Giddings TH Jr, O'Toole ET, Morphew M, Mastronarde DN, McIntosh JR, Winey M (2001). Using rapid freeze and freeze-substitution for the preparation of yeast cells for electron microscopy and three-dimensional analysis. *Methods Cell Biol* 67, 27–42.
- Gupta ML Jr, Bode CJ, Dougherty CA, Marquez RT, Himes RH (2001). Mutagenesis of beta-tubulin cysteine residues in *Saccharomyces cerevisiae*: mutation of cysteine 354 results in cold-stable microtubules. *Cell Motil Cytoskeleton* 49, 67–77.
- Gupta ML Jr, Carvalho P, Roof DM, Pellman D (2006). Plus end-specific depolymerase activity of Kip3, a kinesin-8 protein, explains its role in positioning the yeast mitotic spindle. *Nat Cell Biol* 8, 913–923.
- He Y, Francis F, Myers KA, Yu W, Black MM, Baas PW (2005). Role of cytoplasmic dynein in the axonal transport of microtubules and neurofilaments. *J Cell Biol* 168, 697–703.
- Hebebrand M, Huffmeier U, Trollmann R, Hehr U, Uebe S, Ekici AB, Kraus C, Krumbiegel M, Reis A, Thiel CT, Popp B (2019). The mutational and phenotypic spectrum of TUBA1A-associated tubulinopathy. *Orphanet J Rare Dis* 14, 38.
- Heil-Chapdelaine RA, Oberle JR, Cooper JA (2000). The cortical protein Num1p is essential for dynein-dependent interactions of microtubules with the cortex. *J Cell Biol* 151, 1337–1344.
- Hendricks AG, Perlson E, Ross JL, Schroeder HW 3rd, Tokito M, Holzbaur EL (2010). Motor coordination via a tug-of-war mechanism drives bidirectional vesicle transport. *Curr Biol* 20, 697–702.
- Hu DJ, Baffet AD, Nayak T, Akhmanova A, Doye V, Vallee RB (2013). Dynein recruitment to nuclear pores activates apical nuclear migration and mitotic entry in brain progenitor cells. *Cell* 154, 1300–1313.
- Hughes CS, Foehr S, Garfield DA, Furlong EE, Steinmetz LM, Krijgsveld J (2014). Ultrasensitive proteome analysis using paramagnetic bead technology. *Mol Syst Biol* 10, 757.
- Hwang E, Kusch J, Barral Y, Huffaker TC (2003). Spindle orientation in *Saccharomyces cerevisiae* depends on the transport of microtubule ends along polarized actin cables. *J Cell Biol* 161, 483–488.
- Jaglin XH, Poirier K, Saillour Y, Buhler E, Tian G, Bahi-Buisson N, Fallet-Bianco C, Phan-Dinh-Tuy F, Kong XP, Bomont P, et al. (2009). Mutations in the beta-tubulin gene TUBB2B result in asymmetrical polymicrogyria. *Nat Genet* 41, 746–752.
- Johnson V, Ayaz P, Huddleston P, Rice LM (2011). Design, overexpression, and purification of polymerization-blocked yeast alphabeta-tubulin mutants. *Biochemistry* 50, 8636–8644.
- Kamiyama D, Sekine S, Barsi-Rhynne B, Hu J, Chen B, Gilbert LA, Ishikawa H, Leonetti MD, Marshall WF, Weissman JS, Huang B (2016). Versatile protein tagging in cells with split fluorescent protein. *Nat Commun* 7, 11046.
- Katz W, Weinstein B, Solomon F (1990). Regulation of tubulin levels and microtubule assembly in *Saccharomyces cerevisiae*: consequences of altered tubulin gene copy number. *Mol Cell Biol* 10, 5286–5294.
- Khmelniskii A, Lawrence C, Roostalu J, Schiebel E (2007). Cdc14-regulated midzone assembly controls anaphase B. *J Cell Biol* 177, 981–993.
- Khodiyar VK, Maltais LJ, Ruef BJ, Sneddon KM, Smith JR, Shimoyama M, Cabral F, Dumontet C, Dutcher SK, Harvey RJ, et al. (2007). A revised nomenclature for the human and rodent alpha-tubulin gene family. *Genomics* 90, 285–289.
- Kim Y, Clark DJ (2002). SWI/SNF-dependent long-range remodeling of yeast HIS3 chromatin. *Proc Natl Acad Sci USA* 99, 15381–15386.
- Kosco KA, Pearson CG, Maddox PS, Wang PJ, Adams IR, Salmon ED, Bloom K, Huffaker TC (2001). Control of microtubule dynamics by Stu2p is essential for spindle orientation and metaphase chromosome alignment in yeast. *Mol Biol Cell* 12, 2870–2880.
- Kremer JR, Mastronarde DN, McIntosh JR (1996). Computer visualization of three-dimensional image data using IMOD. *J Struct Biol* 116, 71–76.
- Krogan NJ, Cagney G, Yu H, Zhong G, Guo X, Ignatchenko A, Li J, Pu S, Datta N, Tikuisis AP, et al. (2006). Global landscape of protein complexes in the yeast *Saccharomyces cerevisiae*. *Nature* 440, 637–643.
- Kushnir VV (2000). Rapid and reliable protein extraction from yeast. *Yeast* 16, 857–860.
- Lammers LG, Markus SM (2015). The dynein cortical anchor Num1 activates dynein motility by relieving Pac1/LIS1-mediated inhibition. *J Cell Biol* 211, 309–322.
- Laquerriere A, Maillard C, Cavallin M, Chapon F, Marguet F, Molin A, Sigaudy S, Blouet M, Benoist G, Fernandez C, et al. (2017). Neuropathological hallmarks of brain malformations in extreme phenotypes related to DYNC1H1 mutations. *J Neuropathol Exp Neurol* 76, 195–205.
- Leary A, Sim S, Nazarova E, Shulist K, Genthial R, Yang SK, Bui KH, Francois P, Vogel J (2019). Successive kinesin-5 microtubule crosslinking and sliding promote fast, irreversible formation of a stereotyped bipolar spindle. *Curr Biol* 29, 3825–3837.e3823.
- Lee L, Tirnauer JS, Li J, Schuyler SC, Liu JY, Pellman D (2000). Positioning of the mitotic spindle by a cortical-microtubule capture mechanism. *Science* 287, 2260–2262.
- Lee WL, Oberle JR, Cooper JA (2003). The role of the lissencephaly protein Pac1 during nuclear migration in budding yeast. *J Cell Biol* 160, 355–364.
- Li YY, Yeh E, Hays T, Bloom K (1993). Disruption of mitotic spindle orientation in a yeast dynein mutant. *Proc Natl Acad Sci USA* 90, 10096–10100.
- Liakopoulos D, Kusch J, Grava S, Vogel J, Barral Y (2003). Asymmetric loading of Kar9 onto spindle poles and microtubules ensures proper spindle alignment. *Cell* 112, 561–574.
- Lin H, de Carvalho P, Kho D, Tai CY, Pierre P, Fink GR, Pellman D (2001). Polyploids require Bik1 for kinetochore-microtubule attachment. *J Cell Biol* 155, 1173–1184.
- Lowe J, Li H, Downing KH, Nogales E (2001). Refined structure of alpha beta-tubulin at 3.5 Å resolution. *J Mol Biol* 313, 1045–1057.
- Mahamdeh M, Simmert S, Luchniak A, Schaffer E, Howard J (2018). Label-free high-speed wide-field imaging of single microtubules using interference reflection microscopy. *J Microsc* 272, 60–66.
- Markus SM, Kalutkiewicz KA, Lee WL (2012). She1-mediated inhibition of dynein motility along astral microtubules promotes polarized spindle movements. *Curr Biol* 22, 2221–2230.
- Markus SM, Lee WL (2011). Regulated offloading of cytoplasmic dynein from microtubule plus ends to the cortex. *Dev Cell* 20, 639–651.
- Markus SM, Marzo MG, McKenney RJ (2020). New insights into the mechanism of dynein motor regulation by lissencephaly-1. *eLife* 9, e59737.
- Markus SM, Omer S, Baranowski K, Lee WL (2015). Improved plasmids for fluorescent protein tagging of microtubules in *Saccharomyces cerevisiae*. *Traffic* 16, 773–786.
- Markus SM, Plevock KM, St Germain BJ, Punch JJ, Meaden CW, Lee WL (2011). Quantitative analysis of Pac1/LIS1-mediated dynein targeting: implications for regulation of dynein activity in budding yeast. *Cytoskeleton (Hoboken)* 68, 157–174.
- Marzo MG, Griswold JM, Ruff KM, Buchmeier RE, Fees CP, Markus SM (2019). Molecular basis for dyneinopathies reveals insight into dynein regulation and dysfunction. *eLife* 8, e47246.
- Mastronarde DN (1997). Dual-axis tomography: an approach with alignment methods that preserve resolution. *J Struct Biol* 120, 343–352.
- Mastronarde DN (2005). Automated electron microscope tomography using robust prediction of specimen movements. *J Struct Biol* 152, 36–51.
- Miller RK, Rose MD (1998). Kar9p is a novel cortical protein required for cytoplasmic microtubule orientation in yeast. *J Cell Biol* 140, 377–390.
- Monroy BY, Tan TC, Oclaman JM, Han JS, Simo S, Niwa S, Nowakowski DW, McKenney RJ, Ori-Mckenney KM (2020). A combinatorial MAP code dictates polarized microtubule transport. *Dev Cell* 53, 60–72.e4.
- Morris-Rosendahl DJ, Najm J, Lachmeijer AM, Sztriha L, Martins M, Kuechler A, Haug V, Zeschnigk C, Martin P, Santos M, et al. (2008). Refining the phenotype of alpha-1a tubulin (TUBA1A) mutation in patients with classical lissencephaly. *Clin Genet* 74, 425–433.
- Nazarova E, O'Toole E, Kaitna S, Francois P, Winey M, Vogel J (2013). Distinct roles for antiparallel microtubule pairing and overlap during early spindle assembly. *Mol Biol Cell* 24, 3238–3250.
- Nogales E, Wolf SG, Downing KH (1998). Structure of the alpha beta tubulin dimer by electron crystallography. *Nature* 391, 199–203.
- O'Toole ET, Mastronarde DN, Giddings TH Jr, Winey M, Burke DJ, McIntosh JR (1997). Three-dimensional analysis and ultrastructural design of mitotic spindles from the cdc20 mutant of *Saccharomyces cerevisiae*. *Mol Biol Cell* 8, 1–11.
- O'Toole ET, Winey M, McIntosh JR (1999). High-voltage electron tomography of spindle pole bodies and early mitotic spindles in the yeast *Saccharomyces cerevisiae*. *Mol Biol Cell* 10, 2017–2031.
- O'Toole ET, Winey M, McIntosh JR, Mastronarde DN (2002). Electron tomography of yeast cells. *Methods Enzymol* 351, 81–95.
- Pettersen EF, Goddard TD, Huang CC, Couch GS, Greenblatt DM, Meng EC, Ferrin TE (2004). UCSF Chimera—a visualization system for exploratory research and analysis. *J Comput Chem* 25, 1605–1612.

- Poirier K, Lebrun N, Broix L, Tian G, Saillour Y, Boscheron C, Parrini E, Valence S, Pierre BS, Oger M, et al. (2013). Mutations in TUBG1, DYNC1H1, KIF5C and KIF2A cause malformations of cortical development and microcephaly. *Nat Genet* 45, 639–647.
- Poirier K, Saillour Y, Bahi-Buisson N, Jaglin XH, Fallet-Bianco C, Nabbout R, Castelnaud-Ptakhine L, Roubertie A, Attie-Bitach T, Desguerre I, et al. (2010). Mutations in the neuronal ss-tubulin subunit TUBB3 result in malformation of cortical development and neuronal migration defects. *Hum Mol Genet* 19, 4462–4473.
- Rao AN, Patil A, Black MM, Craig EM, Myers KA, Yeung HT, Baas PW (2017). Cytoplasmic dynein transports axonal microtubules in a polarity-sorting manner. *Cell Rep* 19, 2210–2219.
- Richards KL, Anders KR, Nogales E, Schwartz K, Downing KH, Botstein D (2000). Structure-function relationships in yeast tubulins. *Mol Biol Cell* 11, 1887–1903.
- Saffin JM, Venoux M, Prigent C, Espeut J, Poulat F, Giorgi D, Abrieu A, Rouquier S (2005). ASAP, a human microtubule-associated protein required for bipolar spindle assembly and cytokinesis. *Proc Natl Acad Sci USA* 102, 11302–11307.
- Samora CP, Mogessie B, Conway L, Ross JL, Straube A, McAinsh AD (2011). MAP4 and CLASP1 operate as a safety mechanism to maintain a stable spindle position in mitosis. *Nat Cell Biol* 13, 1040–1050.
- Schatz PJ, Pillus L, Grisafi P, Solomon F, Botstein D (1986a). Two functional alpha-tubulin genes of the yeast *Saccharomyces cerevisiae* encode divergent proteins. *Mol Cell Biol* 6, 3711–3721.
- Schatz PJ, Solomon F, Botstein D (1986b). Genetically essential and nonessential alpha-tubulin genes specify functionally interchangeable proteins. *Mol Cell Biol* 6, 3722–3733.
- Schwartz K, Richards K, Botstein D (1997). BIM1 encodes a microtubule-binding protein in yeast. *Mol Biol Cell* 8, 2677–2691.
- Semenova I, Ikeda K, Resaul K, Kraikivski P, Aguiar M, Gygi S, Zaliapin I, Cowan A, Rodionov V (2014). Regulation of microtubule-based transport by MAP4. *Mol Biol Cell* 25, 3119–3132.
- Shah JV, Flanagan LA, Janmey PA, Leterrier JF (2000). Bidirectional translocation of neurofilaments along microtubules mediated in part by dynein/dynactin. *Mol Biol Cell* 11, 3495–3508.
- Sheeman B, Carvalho P, Sagot I, Geiser J, Kho D, Hoyt MA, Pellman D (2003). Determinants of *S. cerevisiae* dynein localization and activation: implications for the mechanism of spindle positioning. *Curr Biol* 13, 364–372.
- Shigematsu H, Imasaki T, Doki C, Sumi T, Aoki M, Uchikubo-Kamo T, Sakamoto A, Tokuraku K, Shirouzu M, Nitta R (2018). Structural insight into microtubule stabilization and kinesin inhibition by Tau family MAPs. *J Cell Biol* 217, 4155–4163.
- Shima T, Morikawa M, Kaneshiro J, Kambara T, Kamimura S, Yagi T, Iwamoto H, Uemura S, Shigematsu H, Shirouzu M, et al. (2018). Kinesin-binding-triggered conformation switching of microtubules contributes to polarized transport. *J Cell Biol* 217, 4164–4183.
- Sirajuddin M, Rice LM, Vale RD (2014). Regulation of microtubule motors by tubulin isotypes and post-translational modifications. *Nat Cell Biol* 16, 335–344.
- Straight AF, Marshall WF, Sedat JW, Murray AW (1997). Mitosis in living budding yeast: anaphase A but no metaphase plate. *Science* 277, 574–578.
- Tirnauer JS, O'Toole E, Berrueta L, Bierer BE, Pellman D (1999). Yeast Bim1p promotes the G1-specific dynamics of microtubules. *J Cell Biol* 145, 993–1007.
- Toso RJ, Jordan MA, Farrell KW, Matsumoto B, Wilson L (1993). Kinetic stabilization of microtubule dynamic instability in vitro by vinblastine. *Biochemistry* 32, 1285–1293.
- Tsai JW, Lian WN, Kemal S, Kriegstein AR, Vallee RB (2010). Kinesin 3 and cytoplasmic dynein mediate interkinetic nuclear migration in neural stem cells. *Nat Neurosci* 13, 1463–1471.
- Venoux M, Basbous J, Berthenet C, Prigent C, Fernandez A, Lamb NJ, Rouquier S (2008). ASAP is a novel substrate of the oncogenic mitotic kinase Aurora-A: phosphorylation on Ser625 is essential to spindle formation and mitosis. *Hum Mol Genet* 17, 215–224.
- Vissers LE, de Ligt J, Gilissen C, Janssen I, Steehouwer M, de Vries P, van Lier B, Arts P, Wieskamp N, del Rosario M, et al. (2010). A de novo paradigm for mental retardation. *Nat Genet* 42, 1109–1112.
- Wagner OI, Ascano J, Tokito M, Leterrier JF, Janmey PA, Holzbaur EL (2004). The interaction of neurofilaments with the microtubule motor cytoplasmic dynein. *Mol Biol Cell* 15, 5092–5100.
- Westermann S, Avila-Sakar A, Wang HW, Niederstrasser H, Wong J, Drubin DG, Nogales E, Barnes G (2005). Formation of a dynamic kinetochore-microtubule interface through assembly of the Dam1 ring complex. *Mol Cell* 17, 277–290.
- Willemsen MH, Vissers LE, Willemsen MA, van Bon BW, Kroes T, de Ligt J, de Vries BB, Schoots J, Lugtenberg D, Hamel BC, et al. (2012). Mutations in DYNC1H1 cause severe intellectual disability with neuronal migration defects. *J Med Genet* 49, 179–183.
- Winey M, Mamay CL, O'Toole ET, Mastronarde DN, Giddings TH Jr, McDonald KL, McIntosh JR (1995). Three-dimensional ultrastructural analysis of the *Saccharomyces cerevisiae* mitotic spindle. *J Cell Biol* 129, 1601–1615.
- Woodruff JB, Drubin DG, Barnes G (2009). Dynein-driven mitotic spindle positioning restricted to anaphase by She1p inhibition of dynactin recruitment. *Mol Biol Cell* 20, 3003–3011.
- Yin H, Pruyne D, Huffaker TC, Bretscher A (2000). Myosin V orientates the mitotic spindle in yeast. *Nature* 406, 1013–1015.
- Zhu Y, An X, Tomaszewski A, Hepler PK, Lee WL (2017). Microtubule cross-linking activity of She1 ensures spindle stability for spindle positioning. *J Cell Biol* 216, 2759–2775.
- Zimniak T, Stengl K, Mechtler K, Westermann S (2009). Phosphoregulation of the budding yeast EB1 homologue Bim1p by Aurora/Ipl1p. *J Cell Biol* 186, 379–391.